



OPEN

Exploring pyrazolines as potential inhibitors of NSP3-macrodomain of SARS-CoV-2: synthesis and in silico analysis

Rekha Joshi¹, Harsh Gaikwad¹, Bhavana Soge², Abdulrahman Alshammari³, Norah A. Albekairi³, Atul Kabra⁴, Usha Yashwante², Baban Kolte^{5,6}, Pradip Lokhande¹✉ & Rohan J Meshram²✉

COVID-19 has proved to be a global health crisis during the pandemic, and the emerging JN.1 variant is a potential threat. Therefore, finding alternative antivirals is of utmost priority. In the current report, we present the synthesis of new and potential anti-viral pyrazoline compounds. Here we report a chemical scheme where β -aryl β -anilino ketones react with phenyl hydrazine in potassium hydroxide to give the corresponding 3,5-diarylpyrazoline. The protocol is applicable to a variety of β -amino ketones and tolerates several functional groups. This method is efficient and proceeds regioselectivity since the β -Anilino group acts as a protecting group for alkenes of chalcones. We identified the NSP3-macrodomain (Mac-1) of SARS-CoV-2 as a putative target for newly synthesized triaryl-2-pyrazoline compounds. The molecular dynamics simulation-based free energy estimation suggests compounds 7a, 7d, 7g, 7i, 7k, and 7L as promising Mac-1 inhibitors. The detailed structural inspection of MD simulation trajectories sheds light on the structural and functional dynamics involved in the SARS-CoV-2 Mac-1. The data presented here is expected to guide the design and development of better anti-SARS-CoV-2 therapies.

Keywords Regioselective synthesis, NSP3-macrodomain, COVID-omicron XBB variant, Docking, MMPBSA, Linear interaction energy, Molecular dynamics simulations, Triaryl-2-pyrazoline

In the wake of the unprecedented global pandemic caused by the severe acute respiratory syndrome coronavirus 2 (SARS-CoV-2), there has been an urgent and relentless quest to identify effective therapeutic strategies to combat this viral pathogen¹. Covid-19 is estimated to result in more than 6 million fatalities across the globe². The NSP3-macrodomain (Mac1) has emerged as a promising target from extensive research efforts³. NSP3 is a multifunctional protein encoded by the SARS-CoV-2 genome⁴. The NSP3 protein from SARS-CoV-2 consists of three domains: macrodomain (Mac1) along with the two SUD like domains⁵. Mac1 has attracted significant attention due to its pivotal role in viral replication, immune evasion, and host-pathogen interactions^{6–8}. Understanding the Mac1's structural and functional intricacies is therefore critical in deciphering its significance in the SARS-CoV-2 pathophysiology. This domain has been shown to play a central role in the virus's ability to counteract host immune responses, enabling its survival and propagation within the human host⁹. Per se, elucidating the molecular mechanisms underpinning Mac1's inhibition is crucial for designing targeted interventions that can disrupt its function and impede viral replication.

Pyrazoline has recently been recognized as one of the most valuable heterocyclic scaffolds in medicinal chemistry due to its broad spectrum of activity in clinical settings¹⁰. This pharmacophore is established as a critical component in the targeted synthesis of chemicals in the field of synthetic and medicinal chemistry that have a high affinity for various biotargets^{11–13}. Because of their exceptional antioxidant, anti-inflammatory,

¹Department of Chemistry, Savitribai Phule Pune University, Pune, Pune, Maharashtra 411007, India. ²Bioinformatics Centre, Savitribai Phule Pune University, Pune, Maharashtra 411007, India. ³Department of Pharmacology and Toxicology, College of Pharmacy, King Saud University, Post Box 2455, Riyadh 11451, Saudi Arabia. ⁴University Institute of Pharma Sciences, Chandigarh University, Mohali, Punjab, India. ⁵Department of Microbial Genome Research, Leibniz Institute DSMZ – German Collection of Microorganisms and Cell Cultures, 38124 Braunschweig, Germany. ⁶Institute of Microbiology, Technical University of Braunschweig, 38106 Braunschweig, Germany. ✉email: pdlokande@gmail.com; rohan_meshram@rediffmail.com

antifungal, analgesic, antipyretic, antibacterial, antiangiogenic, antiviral, and antitumoral properties, pyrazolinic scaffolds have a wide range of applications in pharmacology^{14–16}. The pyrazoline ring is known to play a significant role in urease and α-glycosidase inhibition¹⁷. Some of the marked drugs are shown in Fig. 1. Regarding SARS-CoV-2 therapeutics, the pyrazoline nucleus has been considered an attractive chemical scaffold. For example, Moon et al. reported covalent inhibitors based on pyrazoline scaffold¹⁸. These compounds were designed to target the main protease of the virus. Similarly, a recent DFT-based analysis identified pyrazoline derivatives as potential spike protein blockers of SARS-CoV-2¹⁹. However, these compounds are yet to be experimentally

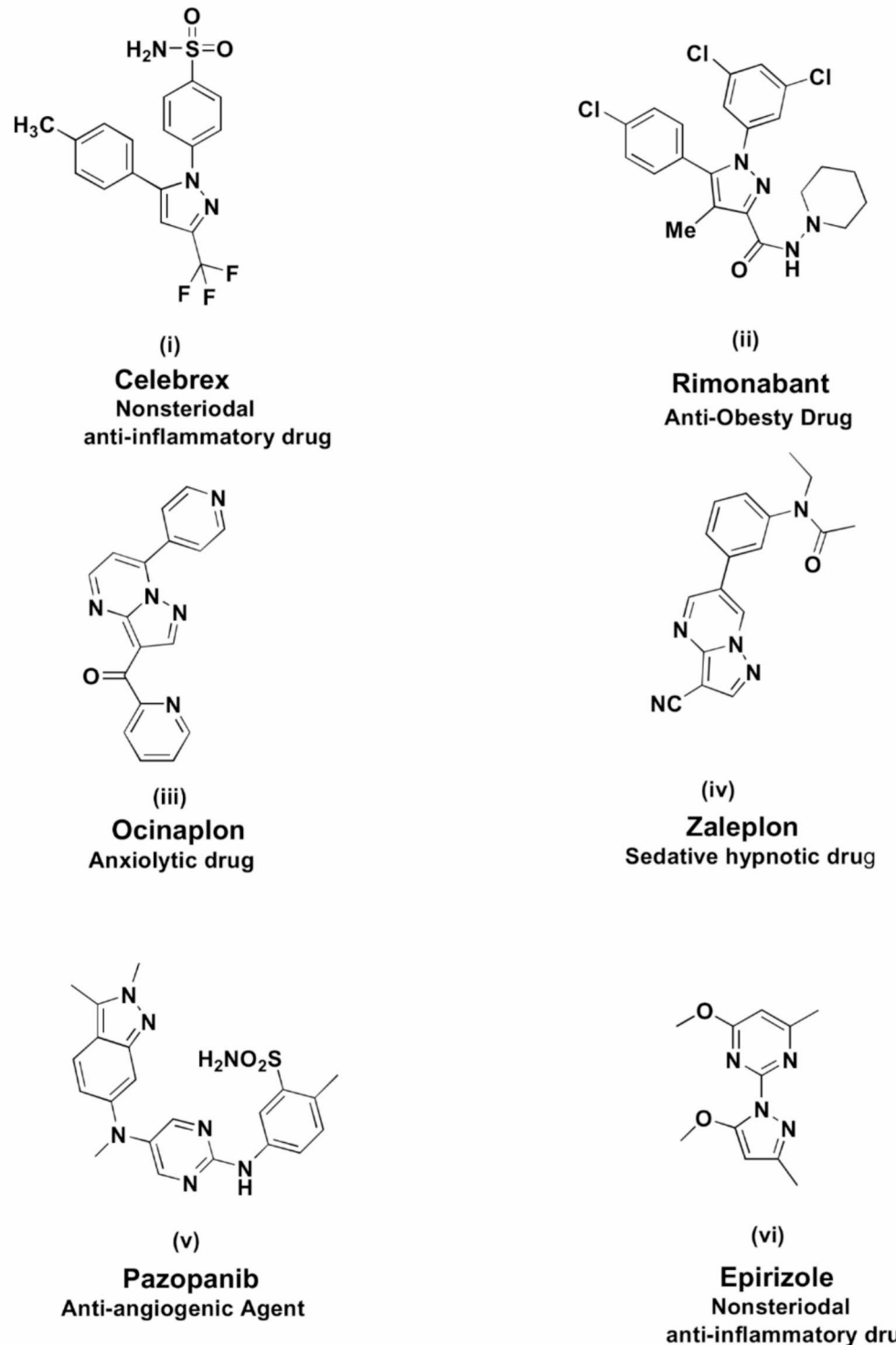


Fig. 1. Structures of pyrazoline-based drugs and their associated bioactivity.

tested. Steroidal pyrazolines were synthesized and tested in silico as main protease inhibitors²⁰. In addition to the literary evidence provided, our decision to focus on modifying the pyrazoline scaffold was primarily influenced by a crystallographic study. This study revealed that an aryl-substituted pyrazole fragment exhibits a modest binding affinity to Mac1²¹.

Extensive research has been conducted on the reactions involving chalcones and phenyl hydrazine, primarily for the synthesis of 3,5-diaryl pyrazoline compounds. In these reactions, the resulting products typically consist of both 3,5-diaryl and 5,3-diaryl isomers, with the distribution of regioisomers being influenced by the electrophilicity of the carbon atoms at positions 1 and 3 in the reactants²². The amine group undergoes a reaction with the carbonyl group to produce an imine, which is followed by the reaction of the aryl-substituted nitrogen with the beta carbon, leading to the formation of pyrazoline. It's worth noting that the reverse reaction pathway can also yield the other Regio isomer²³. These reaction pathways are further influenced by the substituents on the substrate, which can alter the electrophilicity of the carbon atoms at positions 1 or 3. Furthermore, the regioselectivity of the pyrazoline product is also determined by the nucleophilicity of phenyl hydrazine²⁴.

Various synthetic routes for the synthesis of substituted pyrazolines are reported in the literature. For example, synthesis using catalyst and solvent such as glacial acetic acid under heating or ultrasound irradiation²², sodium hydroxide in ethyl alcohol under ultrasound irradiation²⁵. Additionally, various well-established methods have been standardized for the synthesis of pyrazolines. These methods include K_2CO_3 -mediated microwave irradiation²⁶, utilizing glacial acetic acid in ethanol under microwave irradiation^{27,28}. Employing ethanol as a solvent²⁹. Using $SOCl_2$ in benzene under conventional heating³⁰, utilizing $H_3PW_{12}O_40^{31}$, ethyl lactate³² and employing Amberlyst 15 in refluxing toluene³³. Sridhar and Rajendraprasad demonstrated synthesis by utilizing pyridine in refluxing ethanol³⁴. Besides these, utilizing cerium chloride heptahydrate in refluxing ethyl lactate is also reported³⁵. These standardized approaches offer various options for synthesizing pyrazolines, depending on the specific requirements of the reaction. In these reactions, Benzene and DMSO are generally used as the conventional solvents that are known to have impacts on the environment³⁶.

The afore mentioned methods come with certain limitations, such as extended reaction times, relatively modest yields, and the requirement for high temperatures to complete the reactions. More recently, in pursuit of greener chemistry practices, expensive catalysts have been employed for the synthesis of pyrazolines from chalcones. However, a common challenge across these methodologies is the issue of regioselectivity when preparing pyrazolines. This lack of regioselectivity becomes a significant concern, particularly when aiming to synthesize appropriate substitutes for pyrazoles or allied pharmaceutically relevant compounds. From a mechanistic perspective, both Regio isomers are typically formed in these reactions, leading to challenges in product yield and necessitating intricate separation techniques. Consequently, due to the considerable bioavailability and versatile applications of pyrazolines in the field of organic chemistry, there has been a persistent interest in devising straightforward, efficient, and environmentally friendly approaches for their synthesis.

In our previous synthetic attempts, we reported the regioselective synthesis of pyrazoline compounds. This synthesis involved the reaction between chalcones and phenylhydrazine in dimethyl sulfoxide (DMSO), followed by aromatization to form pyrazoles published elsewhere³⁷. In the current report, we aim to introduce a novel approach for the regioselective synthesis of pyrazolines. This approach involves the use of β -amino ketone, with the aniline group acting as a protecting group for the beta carbon of the alkene bond in chalcones. Such regioselective synthesis of pyrazoline from alkene-protected chalcones are rarely reported in the literature.

Furthermore, we tried investigating the potential applications of these newly synthesized pyrazoline compounds in the antiviral therapy. Specifically, we explored their utility as inhibitors of the Mac1 from SARS-CoV-2. We demonstrate an in-silico approach, which allows to computationally analyse the interactions between these pyrazolines and the target protein. The ultimate objective is to offer insights into the development of pyrazoline compounds with potential antiviral properties.

Materials and methods

Chemical synthesis of triaryl-2-pyrazolines

Melting points determined are uncorrected. All solvents used were of reagent grade, and when necessary, were purified and dried by standard methods. Reactions and products were routinely monitored by thin layer chromatography (TLC) on silica gel (Kieselgel 60 F254, Merck). Column chromatographic purifications were performed using 100–200 mesh silica gel. IR spectra were recorded on Nicolet 5700 instrument. The 1H and $^{13}CNMR$ spectra were recorded on Varian and Bruker spectrometer. Chemical shifts (δ) are reported in ppm and with reference to tetramethyl silane as an internal standard.

General procedure for the synthesis of pyrazoline

A mixture of β -amino ketones 4 a-l, (1 mol), phenyl hydrazine 6 (1 mol), and KOH (20 mol%) in ethanol (5 mL) was taken in the round bottom flask and it was allowed to be heated at 40°C for 2–3 h. The completion of the reaction was confirmed by TLC. The reaction mixture was workup in ice-cold water and then filter to get a solid product. After the column chromatographic purification process pyrazoline 7 a-l were obtained as a pale yellow solid. The product was identified by IR¹, H-NMR¹³, C-NMR, and LCMS.

1,3,5-triphenyl-4,5-dihydro-1 H-pyrazole (7a): Yellow Solid, Yield: 92%; IR(KBr) (ν_{max}/cm^{-1}): 771, 1168, 1274, 1558, 1660, 1606, 2920 cm^{-1} ; 1H NMR(400 MHz, $CDCl_3$) δ 3.18 (dd, $J=8, 12$ Hz, 1 H); 3.88 (dd, $J=8, 12$ Hz, 1 H), 5.31 (dd, $J=8, 8$ Hz, 1 H), 7.11 (dd, $J=4, 1.2$ Hz, 2 H), 7.26–7.17 (m, 2 H), 7.45–7.34 (m, 9 H), 7.78–7.72 (m, 2 H)¹³, CNMR (101 MHz, $CDCl_3$) δ 43.6, 64.5, 113.4, 125.3, 125.7, 127.4, 127.5, 128.7, 128.8, 128.9, 129.2, 132.7, 140.1, 142.6, 151.9; MS (EI, 70eV) m/z 298.15 (M^+).

5-(4-chlorophenyl)-1,3-diphenyl-4,5-dihydro-1 H-pyrazole (7b): Yellow Solid, IR(KBr) (ν_{max}/cm^{-1}): 1168, 1274, 1558, 1660, 1606, 2920 cm^{-1} ; 1H NMR (400 MHz, $CDCl_3$) δ 3.13 (dd, $J=12, 8$ Hz, 1 H); 3.87 (dd, $J=12, 8$ Hz, 1 H), 5.28 (dd, $J=8, 8$ Hz, 1 H), 6.85 (dd, $J=7.3, 1.0$ Hz, 1 H), 7.13–7.03 (m, 2 H), 7.22 (dd, $J=8, 4.2$ Hz,

2 H), 7.46–7.28 (m, 7 H), 7.80–7.70 (m, 2 H)¹³, C NMR (101 MHz, CDCl₃) δ 43.5, 63.9, 119.3, 125.7, 127.3, 128.6, 128.7, 128.9, 129.3, 132.5, 133.3, 141.1, 144.6, 146.7, 156.3; MS (EI, 70eV) m/z 332.11 (M⁺).

5-(2-chlorophenyl)-1,3-diphenyl-4,5-dihydro-1 H-pyrazole (7c) : Yellow Solid, IR (KBr) ($\nu_{\text{max}}/\text{cm}^{-1}$): 1168, 1274, 1558, 1660, 1606, 2920 cm⁻¹; ¹H NMR (400 MHz, CDCl₃) δ 3.13 (dd, J=12, 8 Hz, 1 H), 3.87 (dd, J=12, 8 Hz, 1 H); 5.28 (dd, J=8, 8 Hz, 1 H), 6.85 (dd, J=7.3, 1.0 Hz, 1 H), 7.13–7.03 (m, 2 H), 7.22 (dd, J=8, 1.0 Hz, 1 H), 7.46–7.28 (m, 8 H), 7.80–7.70 (m, 2 H)¹³, C NMR (101 MHz, CDCl₃) δ 43.5, 63.9, 117.6, 124.5, 125.78, 126.9, 127.3, 128.5, 128.6, 129.3, 129.5, 130.3, 132.5, 134.0, 136.8, 142.2, 156.2; MS (EI, 70eV) m/z 332.11 (M⁺).

5-(4-bromophenyl)-1,3-diphenyl-4,5-dihydro-1 H-pyrazole (7d) : Yellow Solid, IR (KBr) ($\nu_{\text{max}}/\text{cm}^{-1}$): 692, 759, 873, 1125, 1325, 1394, 1504, 1596, 3022 cm⁻¹; ¹H NMR (400 MHz, CDCl₃) δ 3.13 (dd, J=12, 8 Hz, 1 H), 3.86 (dd, J=12, 8 Hz, 1 H), 5.26 (dd, J=8, 8 Hz, 1 H), 7.14–7.24 (m, 3 H), 7.28 (d, J=8 Hz, 1 H), 7.30–7.42 (m, 6 H), 7.35–7.48 (m, 2 H), 7.80 (d, J=7.8 Hz, 2 H); ¹³C NMR (101 MHz, CDCl₃) δ 43.4, 63.9, 119.4, 121.4, 125.7, 127.7, 128.6, 128.7, 129.0, 132.3, 132.5, 141.6, 144.6, 146.7, 156.3; MS (EI, 70eV) m/z 376.06 (M⁺).

5-(4-methoxyphenyl)-1,3-diphenyl-4,5-dihydro-1 H-pyrazole (7e) : Yellow Solid, IR (KBr) ($\nu_{\text{max}}/\text{cm}^{-1}$): 692, 759, 873, 1125, 1325, 1394, 1504, 1596, 3022 cm⁻¹; ¹H NMR (400 MHz, CDCl₃) δ 3.16 (dd, J=12, 8 Hz, 1 H), 3.61 (dd, J=12, 8 Hz, 1 H), 3.86 (s, 3 H), 5.27 (dd, J=8, 8 Hz, 1 H), 6.87 (d, J=8 Hz, 1 H), 6.93 (d, J=8 Hz, 1 H), 7.16–7.33 (m, 6 H), 7.35–7.48 (m, 4 H), 7.80 (d, J=7.8 Hz, 2 H); ¹³C NMR (101 MHz, CDCl₃) δ 43.6, 55.3, 64.0, 113.5, 114.5, 119.1, 125.8, 127.1, 128.6, 128.9, 132.9, 134.7, 144.9, 146.8, 156.3, 159.0; MS (EI, 70eV) m/z 328.16 (M⁺).

1,5-diphenyl-3-(p-tolyl)-4,5-dihydro-1 H-pyrazole (7f) : Yellow Solid, IR (KBr) ($\nu_{\text{max}}/\text{cm}^{-1}$): 692, 759, 873, 1125, 1325, 1394, 1504, 1596, 3022 cm⁻¹; ¹H NMR (400 MHz, CDCl₃) δ 2.41 (s, 1 H), 3.16 (dd, J=12, 8 Hz, 1 H), 3.85 (dd, J=12, 8 Hz, 1 H), 5.28 (dd, J=8, 8 Hz, 1 H), 6.81 (m, 1 H), 7.11 (dd, J=8.1, 1.0 Hz, 2 H), 7.26–7.17 (m, 4 H), 7.32–7.27 (m, 1 H), 7.37 (d, J=4 Hz, 4 H), 7.66 (d, J=8.1 Hz, 2 H); ¹³C NMR (101 MHz, CDCl₃) δ 21.4, 43.7, 64.5, 118.9, 125.7, 125.9, 127.5, 127.8, 128.5, 128.9, 129.28, 130.0, 138.7, 142.7, 146.9, 156.2; MS (EI, 70eV) m/z 312.41 (M⁺).

3-(4-chlorophenyl)-5-(4-methoxyphenyl)-1-phenyl-4,5-dihydro-1 H-pyrazole (7 g) : Yellow Solid, IR (KBr) ($\nu_{\text{max}}/\text{cm}^{-1}$): 771, 1168, 1274, 1558, 1660, 1606, 2920 cm⁻¹; ¹H NMR (400 MHz, CDCl₃) δ 3.11 (dd, J=12, 8 Hz, 1 H), 3.61 (dd, J=12, 8 Hz, 1 H), 3.86 (s, 3 H), 5.27 (dd, J=8, 8 Hz, 1 H), 6.84–6.58 (m, 1 H), 7.11–7.28 (m, 6 H), 7.45–7.31 (m, 5 H), 7.78 (d, J=8 Hz, 1 H); ¹³C NMR (101 MHz, CDCl₃) δ 43.4, 55.2, 64.1, 114.5, 119.3, 125.3, 127.5, 128.7, 128.8, 128.9, 131.3, 134.4, 144.5, 156.4, 159.0, MS (EI, 70eV) m/z 362.12 (M⁺).

1-phenyl-3,5-di-p-tolyl-4,5-dihydro-1 H-pyrazole (7 h) : Yellow Solid, IR (KBr) ($\nu_{\text{max}}/\text{cm}^{-1}$): 692, 759, 873, 1125, 1325, 1394, 1504, 1596, 3022 cm⁻¹; ¹H NMR (400 MHz, CDCl₃) δ 2.35 (s, 3 H), 2.40 (s, 3 H), 3.15 (dd, J=12, 8 Hz, 1 H), 3.83 (dd, J=12, 8 Hz, 1 H), 5.24 (dd, J=8, 8 Hz, 1 H), 6.87–6.71 (m, 1 H), 7.31–7.05 (m, 10 H), 7.64 (d, J=8.0 Hz, 2 H)¹³, C NMR (101 MHz, CDCl₃) δ 21.1, 21.4, 43.7, 64.2, 113.3, 118.8, 125.7, 125.8, 128.8, 128.9, 129.2, 129.7, 137.1, 138.6, 139.7, 145.1, 156.4; MS (EI, 70eV) m/z 326.18 (M⁺).

3,5-bis(4-chlorophenyl)-1-phenyl-4,5-dihydro-1 H-pyrazole (7i) : Yellow Solid, IR (KBr) ($\nu_{\text{max}}/\text{cm}^{-1}$): 771, 1168, 1274, 1558, 1660, 1606, 2920 cm⁻¹; ¹H NMR (400 MHz, CDCl₃) δ 3.09 (dd, J=12, 8 Hz, 1 H), 3.83 (dd, J=12, 8 Hz, 1 H), 5.29 (dd, J=8, 8 Hz, 1 H), 6.84 (t, J=8 Hz, 1 H), 7.06 (dd, J=7.8, 1.0 Hz, 2 H), 7.30–7.15 (m, 4 H), 7.42–7.28 (m, 4 H), 7.66 (d, J=8.7 Hz, 2 H); ¹³C NMR (101 MHz, CDCl₃) δ 43.3, 64.0, 114.1, 119.6, 126.9, 127.3, 128.8, 129.0, 129.4, 131.0, 131.7, 134.4, 140.8, 144.3, 156.3; MS (EI, 70eV) m/z 366.05 (M⁺).

3-(4-chlorophenyl)-1-(4-fluorophenyl)-5-(p-tolyl)-4,5-dihydro-1 H-pyrazole (7j) : Yellow Solid, IR (KBr) ($\nu_{\text{max}}/\text{cm}^{-1}$): 771, 1168, 1274, 1558, 1660, 1606, 2920 cm⁻¹; ¹H NMR (400 MHz, CDCl₃) δ 2.36 (s, 3 H), 3.11 (dd, J=12, 8 Hz, 1 H), 3.81 (dd, J=12, 8 Hz, 1 H), 5.21 (dd, J=8, 8 Hz, 1 H), 6.95–6.85 (m, 2 H), 7.05–6.97 (m, 2 H), 7.20 (m, 4 H), 7.37 (d, J=8.6 Hz, 2 H), 7.65 (d, J=8.6 Hz, 2 H)¹³, C NMR (101 MHz, CDCl₃) δ 21.1, 43.6, 65.1, 114.6, 115.5, 125.8, 126.8, 128.9, 129.9, 131.2, 134.3, 137.5, 138.3, 139.1, 155.8, 158.1; MS (EI, 70eV) m/z 364.11 (M⁺).

1-(4-fluorophenyl)-5-phenyl-3-(p-tolyl)-4,5-dihydro-1 H-pyrazole (7k) : Yellow Solid, IR (KBr) ($\nu_{\text{max}}/\text{cm}^{-1}$): 692, 759, 873, 1125, 1325, 1394, 1504, 1596, 3022 cm⁻¹; ¹H NMR (400 MHz, CDCl₃) δ 2.40 (s, 3 H), 3.16 (dd, J=12, 8 Hz, 1 H), 3.85 (dd, J=12, 8 Hz, 1 H), 5.20 (dd, J=8, 8 Hz, 1 H), 6.95–6.80 (m, 3 H), 7.24–6.98 (m, 7 H), 7.79–7.61 (m, 3 H); ¹³C NMR (101 MHz, CDCl₃) δ 21.4, 43.7, 64.2, 113.3, 118.8, 125.7, 125.8, 128.8, 129.2, 129.7, 137.1, 138.6, 139.7, 145.1, 146.9, 156.2; MS (EI, 70eV) m/z 330.15 (M⁺).

3-(4-chlorophenyl)-1,5-di-p-tolyl-4,5-dihydro-1 H-pyrazole (7L) : Yellow Solid, IR (KBr) ($\nu_{\text{max}}/\text{cm}^{-1}$): 692, 759, 873, 1125, 1325, 1394, 1504, 1596, 3022 cm⁻¹; ¹H NMR (400 MHz, CDCl₃) δ 2.26 (s, 3 H); 2.35 (s, 3 H), 3.12 (dd, J=12, 8 Hz, 1 H), 3.78 (dd, J=12, 8 Hz, 1 H), 5.24 (dd, J=8, 8 Hz, 1 H), 7.21–7.15 (m, 4 H), 7.24–7.30 (m, 2 H), 7.30–7.42 (m, 2 H), 7.52 (d, J=8.4 Hz, 2 H), 7.57–7.70 (m, 2 H)¹³, C NMR (101 MHz, CDCl₃) δ 21.2, 43.4, 64.7, 117.0, 127.0, 127.5, 129.8, 129.5, 131.5, 134.0, 134.8, 135.3, 137.2, 139.5, 142.6, 156.2; MS (EI, 70eV) m/z 360.14 (M⁺).

The overall methodology for performing the in silico analysis is pictorially represented in Fig. 2 below.

In silico molecular docking

An already standardized protocol for molecular docking and virtual screening was used in this study that is published elsewhere^{38–41}. The following section briefly summarizes the major steps involved in performing molecular docking and virtual screening.

Compound preparation

The 2D structures of the compounds were initially drawn in the ChemDraw Ultra software and their SMILES were obtained⁴². Subsequently, OpenBabelGUI⁴³ was used to generate the 3D coordinates of the compounds in SDF format taking the SMILES as input from the previous step. The 3D conformers obtained from OpenBabel are usually not in their lowest energy states. Therefore, these compounds were subjected to an energy minimization procedure prior to virtual screening. The compounds were energy minimized using the Conjugate Gradient optimization algorithm applying UFF forcefield⁴⁴ for initially 400 steps. If required, the optimization process

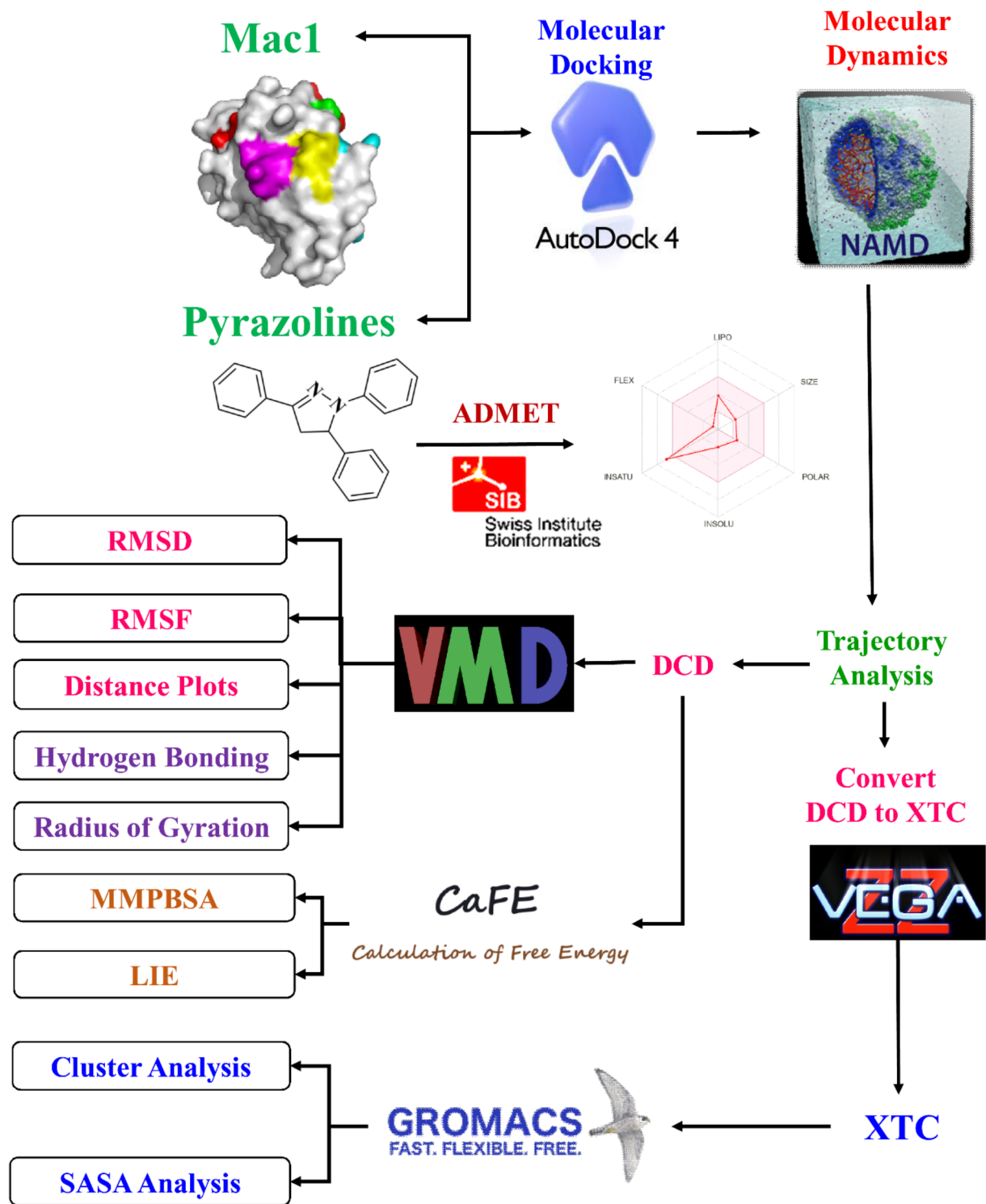


Fig. 2. Pictorial overview of the study's methodology.

was continued beyond 400 steps until the compound achieved its lowest energy state. The energy minimization and optimization was conducted using the ‘Minimize selected’ command from the Python Prescription (PyRx) environment⁴⁵. Finally, the compounds were converted to the pdbqt format for the subsequent molecular docking procedure using the ‘Convert All to AutoDock Ligand (pdbqt)’ command from PyRx.

Receptor preparation

The coordinates of the receptor molecule were obtained from PDB with the identifier 5S3I. This model corresponds to the NSP3-microdomain of SARS-CoV-2 co-crystallized with the aryl-pyrazoline inhibitor (Z50145861)²¹. The choice of using structural model with PDB identifier 5S3I was made on the dual fact that the model was co-crystallized with the pyrazoline fragment and was crystallized with high resolution of 1.17 Å. The downloaded coordinate file consists of two identical chains. Therefore, a single chain was saved into a separate file. For the sake of docking system validation, the co-crystallized inhibitor was separated from the complex, and the macrodomain was saved in its apo-form (i.e. only the protein component). Chain and co-crystallized inhibitor separation was performed using software SPDBV 4.0⁴⁶. Subsequently, the target molecule was converted to pdbqt format using the ‘Make macromolecule’ command from PyRx.

System validation and virtual screening

For performing virtual screening, AutoDock 4.2^{47,48} software embedded in PyRx was used. Prior to virtual screening, the docking software was validated by redocking the crystallized ligand (a positive control) back into the binding site of the SARS-CoV-2 NSP3-microdomain. The docking system is assumed to be validated if it can successfully predict the crystallographic pose. Typically, if the Root Mean Square Deviation (RMSD) value between the experimental crystallographic pose and the predicted pose is observed below 2 Å, then it is an indication of successful validation^{38,49}. For validation, initially, a grid of 50 points in the x, y, and z dimensions was set to ensure that the entire binding site was covered in the prediction. The grid was set using the AutoGrid program placing the center of the grid box on the center of gravity of the ligand. The lamarkian genetic algorithm was used for the pose prediction keeping the remaining docking parameters to default values. The resulting 0.83 Å RMSD between the crystallographic and experimental pose demonstrated the consistency and reliability of AutoDock software (Supplementary Fig. 1). The same setting was used for the virtual screening of the test compounds.

Post processing of the docking results

AutoDock provides the output predicted poses in the form of docking log files (dlg files). For the sake of subsequent interaction analysis, all the docked poses were exported into an sdf file and the best pose (the one with the lowest binding free energy) was separated into an sdf file. The exporting task was done using the ‘Save as sdf’ command from the ‘Analyze Results’ menu of PyRx and the best pose separation was performed using NotePad ++ v7.8.8. This best pose in sdf file was converted to pdb file format using OpenBabelGUI software. Later on, its coordinates were merged into the apo-form of the receptor file to generate the receptor-ligand complex using a text editor (NotePad ++ v7.8.8). The receptor-ligand complexes were visualized and the 2D interaction plots were saved as images using Biovia Discovery Studio Visualizer v 21.1.0.20298. The 3D images were rendered using the latest version of the PyMol Software.

MD simulations

All MD simulations were carried out using NAMD⁵⁰. The conventional molecular dynamics (CMD) simulations were performed separately for ligands bound with protein and ligands in free form using CHARMM 22 force field^{51,52}. The topologies and parameters for the ligand were obtained from SwissParam Server⁵³. A well-established protocol from our lab was used to conduct MD simulations that are published elsewhere^{38,49}. In brief, following the CMD convention, the systems were initially subjected to energy minimization for 6000 steps of the conjugate-gradient optimization algorithm. Subsequently, the temperature was gradually raised to 300 K in a 300 ps simulation. The temperature was incremented by 0.001 at each integration step to reach the desired physiological temperature. In the next step, an equilibration simulation was performed for 1 ns keeping constant pressure and temperature. Periodic boundary conditions were set to maintain constant temperature and pressure. The constant temperature was maintained by applying various Langevin Parameters. For example, the damping coefficient was set to 1 applying the damping coefficient to non-hydrogen atoms. The atoms influenced by Langevin dynamics were adjusted to 300 K. Pressure was calculated by kinetic energy and pseudo-molecular virial energy that was based on hydrogen groups. To make this happen, the SHAKE algorithm was used to constrain the bond length containing hydrogen atoms with a tolerance of 0.00001 Angstrom. The hybrid Nosé-Hoover Langevin piston method was used for pressure control. Various features using this method were applied during the simulation. For example, the target pressure for the Langevin piston was set up to 1.01325 bar to model general atmospheric pressure. The barostat oscillation time scale was set up to 100 fs and appropriately, the barostat damping time scale was set to 50 fs to maintain the right balance so that the underdamped dynamics can be avoided and at the same time piston period do not reach exponential decay value. The barostat noise temperature of the piston was set to 300 because the temperature of the simulation is to be maintained at 300 K. The actual equilibration was carried out by regularly rescaling the temperature during the simulation. Temperature rescaling was done after every one fs and simultaneously all velocities were periodically rescaled to 300 K. The production run of 100 ns was carried out with a time step of 2 ns and velocity rescaling was turned off during this stage. Particle Mesh Ewald was used to calculate the nonbonded interactions. To ensure the robustness and reproducibility of the MD simulations, we conducted triplicate 100 ns simulations for each protein-ligand complex. The simulations were performed using the same initial conditions and parameters as described previously, ensuring consistency across replicates. The MD simulations were carried out using the same force field at the same temperature and pressure conditions. The production runs were extended to 100 ns for each of the three independent replicas. The standard deviation of RMSD across these replicates was plotted and found to be well below 0.5 Å for all complexes (Supplementary Fig. 2). This low standard deviation indicates high consistency and reproducibility of the MD results, suggesting that 100 ns simulations are sufficient to capture the essential conformational dynamics of the systems under investigation.

Trajectory analysis

The elementary trajectory analysis was conducted to monitor conformational stability and flexibility by plotting the RMSD, Root Mean Square Fluctuation (RMSF) and Radius of Gyration (RG) profiles along the course of the simulations. The RMSD, RMSF and RG values were extracted from the trajectories using the VMD visualization software v 1.9.4⁵⁴ using the tool command language scripts written in house. Backbone atoms were considered for calculating RMSD with respect to the first frame as a reference. The flexibility of the protein-ligand was monitored by calculating RMSF. The resulting values of RMSD and RMSF were plotted in the time scale of ps.

Hydrogen bonding analysis

The hydrogen bond analysis was performed using the ‘Hydrogen Bond’ plugin from VMD. The focus was given to all hydrogen bonds that originates from the ligand molecule. The donor-acceptor distance was set to 3.0 Å and the hydrogen bond angle cutoff was set to 20 degrees to ensure inclusion of strong hydrogen bonds between protein and ligands in the trajectory analysis.

Cluster analysis and SASA analysis

The cluster command from Gromacs-2023⁵⁵ was used to perform the cluster analysis. Since the simulations were done using NAMD, the output DCD trajectory files were converted to Gromacs readable XTC format employing VEGAZZ v 3.2.3.28 software⁵⁶. During the format conversion, VEGAZZ assigns the default zero number to each frame in the trajectory. Therefore, the ‘trjconv’ command was used to renumber the frames appropriately in the trajectory, which was then subjected to both cluster analysis and SASA analysis. The RMSD cutoff of 0.11 nm was used in this analysis and the middle frame was considered the most representative confirmation of the protein-ligand system in the simulation. For interaction analysis, the representative confirmation was extracted in a separate PDB file using the trjconv command from Gromacs. The interactions were observed in Biovia Discovery Studio Visualizer v 21.1.0.20298 software. The 2D interaction plot obtained at this point was compared to the 2D interaction plot obtained from docking results. Such a comparison provides structural insight into changes that happened in the protein-ligand complex during the course of the simulation. Gromacs command ‘sasa’ was used to perform SASA analysis focusing on the ligand’s surface area.

Free energy estimation

The three most popular endpoint methods, Molecular Mechanics Poisson–Boltzmann Surface Area (MMPBSA), Molecular Mechanics with Generalized Born and Surface Area (MMGBSA) and Linear Interaction Energy (LIE) were used in free energy estimation calculations. Café 1.0 plugin was used for this purpose that effectively implements MMPBSA and LIE methods⁵⁷. Café 1.0 is an effective plugin that works in the form of TCL scripts integrated into the VMD software. On the other hand, MMGBSA was analysis was done using the MM-GBSA method implemented in Prime module of the Schrödinger software⁵⁸. This section concisely summarizes the methodology of these free energy estimation techniques. The structural data required for the free energy calculations were sampled from the final 100 frames of the trajectory when the system is generally well converged.

MMPBSA

The general equation in MMPBSA calculation can be expressed as.

$$\Delta G_{BIND} = \Delta H - T\Delta S = \Delta E_{MM} + \Delta G_{Sol} - T\Delta S \quad (1)$$

Here terms for the gas-phase molecular mechanics (MM) energy, polar solvation free energy (ΔG_{Sol}) can be expressed as follows:

$$\Delta E_{MM} = \Delta E_{INT} + \Delta E_{ELE} + \Delta E_{VDW} \quad (2)$$

$$\Delta G_{Sol} = \Delta G_{PB} + \Delta G_{SA} \quad (3)$$

The molecular mechanics individual components (change in the internal energy, change in electrostatic energy, and change in van der Waal’s energy in Eq. 2) are ensemble properties that were extracted from the trajectory using NAMD. Similarly, the individual components for calculating polar solvation-free energy were estimated using the APBS program⁵⁹. The general equation for calculating the Poisson-Boltzmann equation is expressed in Eq. 4 below.

$$\nabla \cdot \varepsilon(r) \nabla \varphi(r) = -4\pi\rho(r) \quad (4)$$

The surface area contribution in Eq. 3 was obtained from the trajectories using VMD by Eq. 5 as follows.

$$\Delta G_{SA} = \gamma \cdot SASA + b \quad (5)$$

Owing to the computationally intensive calculations involved in the entropic term estimation in Eq. 1, this $T\Delta S$ term is generally not included in MMPBSA method⁶⁰.

LIE

The general equation of LIE calculation can be expressed as shown in Eq. 6 below.

$$\Delta G = \alpha(\langle Vdw \rangle_{bound} - \langle Vdw \rangle_{free}) + \beta(\langle Ele \rangle_{bound} - \langle Ele \rangle_{free}) + \gamma \quad (6)$$

As per LIE ideology, the ensemble properties like van der Waal's and electrostatic contribution are considered in both ligands bound and un-bound states⁶¹. The α , β , and γ are called as empirical parameters. The ensemble components denoted within < > brackets in Eq. 6 were extracted from the trajectories using VMD; while default values for the empirical parameters from Café plugin were used here.

MMGBSA

The Prime module of the Schrödinger software employ the VSGB solvation model, provided more accurate binding energy calculations and reduced the risk of false-positive predictions, enhancing the reliability of the binding affinity estimates. The binding free energy (ΔG_{bind}) was calculated using the following equations⁶².

$$\Delta G_{bind} = \Delta H - T\Delta S \approx \Delta E_{MM} + \Delta G_{sol} - T\Delta S \quad (7)$$

$$\Delta E_{MM} = \Delta E_{internal} + \Delta E_{ele} + \Delta E_{vdw} \quad (8)$$

$$\Delta G_{sol} = \Delta G_{SA} + \Delta G_{GB} \quad (9)$$

ADMET study

In the final phase of the study, the top performing compounds from the end point energy estimation were promoted for the ADMET studies. The ADMET studies were conducted using the SWISS ADME server⁶³. In view of the following advantages, SWISS ADME server was used in the current study. Swiss ADME offers a robust platform for the comprehensive analysis of ADMET properties, covering crucial aspects such as absorption, distribution, metabolism, and excretion. The tool provides a detailed examination of the pharmacokinetic and pharmacodynamic profiles of compounds, aiding in the identification of potential issues early in the drug development process⁶⁴. Moreover, Swiss ADME has established a reputation for delivering accurate and reliable predictions⁶³. The underlying models are based on extensive datasets and rigorous validation processes, instilling confidence in the generated results⁶⁵. This accuracy is crucial for making informed decisions about the viability and potential success of the synthesized compounds in the subsequent drug development pipeline.

Toxicity study

A thorough toxicity assessment of compounds 7a, 7i, 7k, and 7 L utilizing in silico predictive models offered in an online web server ProTox 3 was utilized in this study⁶⁶. ProTox 3 server performs toxicity analysis across various organ toxicity endpoints, toxicity end points, various Tox21 nuclear receptor signaling pathways, molecular initiating events, and metabolism. The compound's potential toxicity was evaluated for hepatotoxicity, neurotoxicity, nephrotoxicity, respiratory toxicity, cardiotoxicity, carcinogenicity, immunotoxicity, mutagenicity, cytotoxicity, BBB-barrier permeability, ecotoxicity, clinical toxicity, and nutritional toxicity. Additionally, its interactions with nuclear receptor signaling pathways including Aryl hydrocarbon Receptor (AhR), Androgen Receptor (AR), Estrogen Receptor Alpha (ER), Peroxisome Proliferator Activated Receptor Gamma (PPAR-Gamma), among others, were examined. Molecular initiating events such as thyroid hormone receptor activation, GABA receptor interaction, and cytochrome P450 metabolism were also considered.

Result and discussion

Chemical synthesis of Triaryl-2-pyrazoline derivatives

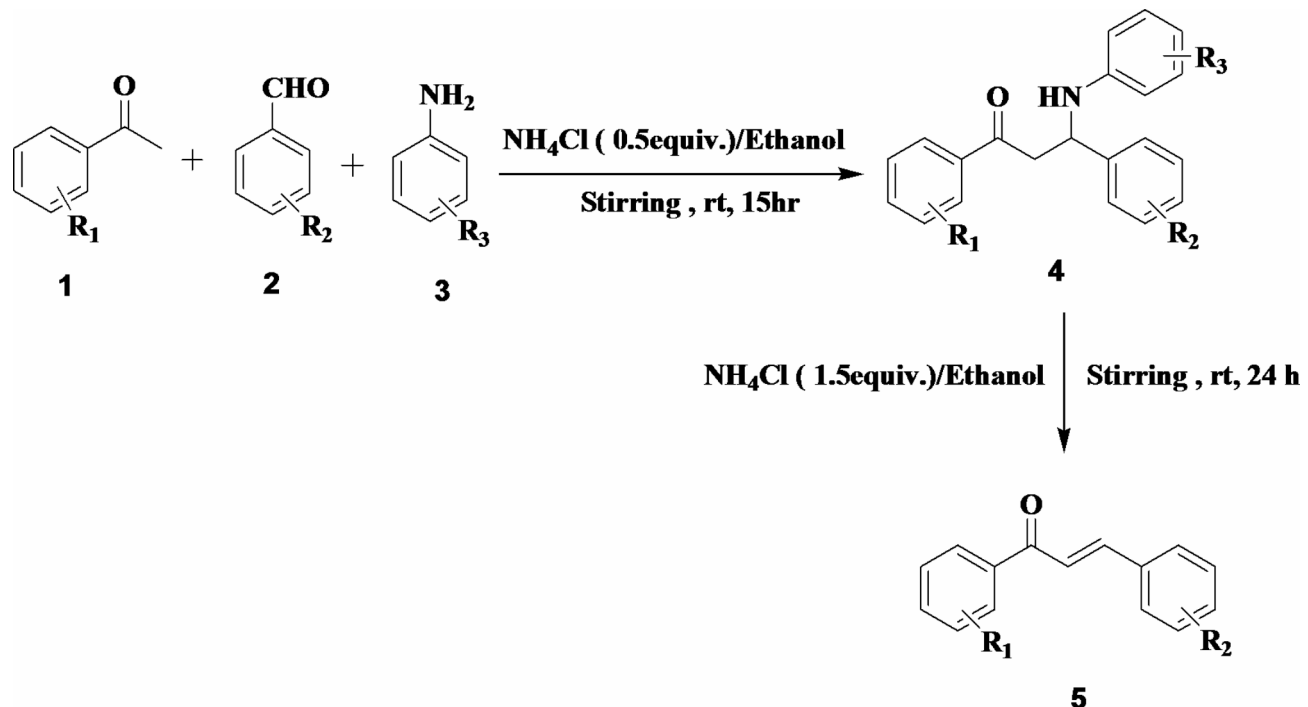
In the present work, we commenced our strategy with the synthesis of β -amino ketones from a multicomponent Mannich type of reaction using aryl aldehydes, acetophenones, and anilines. Ammonium chloride was used as a Bronsted acid which assists the formation of Schiff base from aniline and aryl aldehydes. These Schiff bases further reacted with enolized acetophenones to give β -amino ketones. When these reactions are stirred for a longer time, the chalcones are formed. Elimination of amines from Mannich bases by using acids was reported earlier; but due to difficulties in the protection mechanism of double bonds in alpha beta-unsaturated ketones, this method is rarely reported in the recent literature. Therefore, we synthesized chalcones from β -amino ketone by the methodology depicted in the Scheme 1 below and the results are summarized in Table 1.

These results promoted us to use β -amino ketones as aniline-protected chalcones for the regioselective synthesis of pyrazolines.

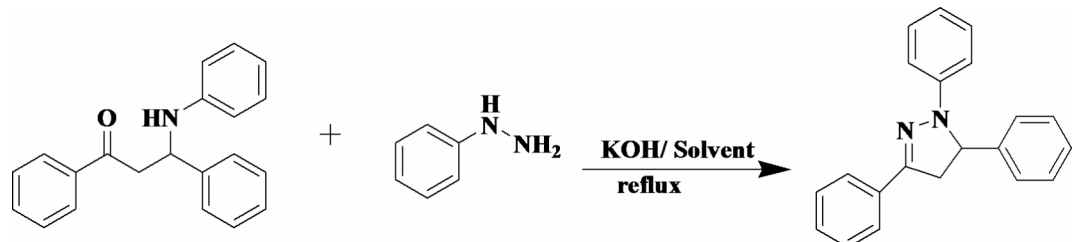
Continuing our studies on the synthesis of pyrazoline, pyrazole, and related compounds from chalcones, here we report the formation of 1,3,5-triaryl-2-pyrazolines by the condensation of β -amino ketones and phenyl hydrazine in the heated ethanol for 3 h using KOH as a catalyst³³. Various catalysts were tested in the synthesis of 1,3,5-triaryl-2-pyrazolines, but KOH in ethanol (EtOH) was found to be advantageous over the remaining. Moreover, the reaction with higher yields were observed. (Scheme 2).

To identify suitable conditions for the reaction, a series of catalysts were screened as shown in Table 2.

Initially the starting material 1,3-diphenyl-3-(phenylamino) propan-1-one (1mmol) has previously been prepared and characterized spectrally and treated with phenyl hydrazine (1mmol) in absence of a catalyst, the reaction did not afford the desired product (Table 2). The appropriate bases for the model reaction were investigated. Initially, when the model reaction was carried out with K_2CO_3 in ethanol, the desired product was produced with an 80% yield. Further, for other base catalysts including trimethylamine (Et3N) and pyridine, the desired product was obtained in 65 and 68% yields in 6 h at 40 °C, respectively. However, when sodium carbonate (Na_2CO_3), and sodium acetate (CH_3COONa), were used as the catalyst, showed the lowest reactivity in the reaction with the lowest yield of only 25 and 20% respectively. When the reaction was carried out in

**Scheme 1.** Synthesis of chalcones from β -amino ketone.

Sr. no.	R ₁	R ₂	Deamination product	Yield (%)
1	H	H	5a	80
2	NO ₂	H	5b	68
3	CH ₃	H	5c	75
4	H	OH	5d	75
5	H	Cl	5e	72
6	H	CH ₃	5f	75
7	Cl	H	5g	48

Table 1. Summary of ammonium chloride catalysed synthesis of β -amino ketone and deamination.**Scheme 2.** The model reaction between β -amino ketones and phenylhydrazine.

presence of potassium hydroxide (KOH) in ethanol, the yield was increased up to 92%. As a result, KOH was determined as the best catalyst for this synthesis.

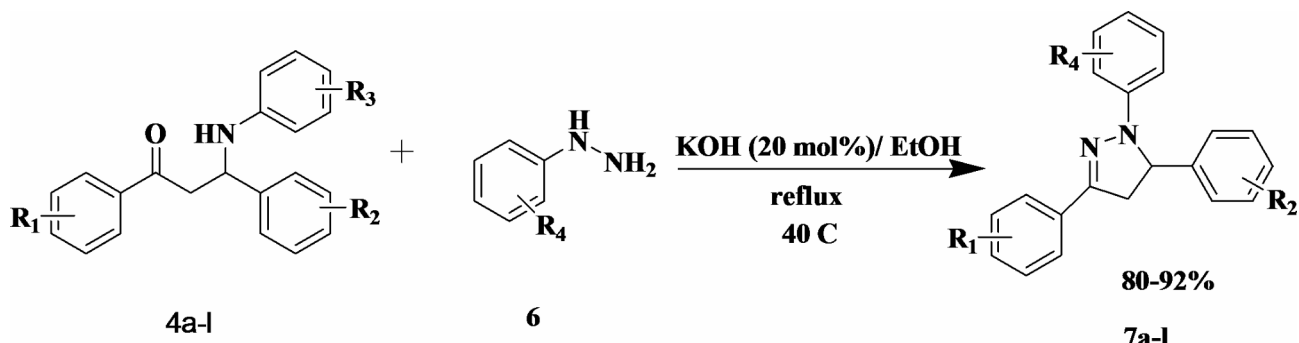
Further reaction optimization suggested that solvents had a strong effect on this process. Thus, a variety of solvents, such as tetrahydrofuran, ethanol, dichloromethane, polyethylene glycol, DMSO, DMF, and dioxane using KOH as a base catalyst at 40 °C were screened (Table 3). In absence of the solvent, the reaction did not proceed indicating the reaction needs to be run in presence of a solvent. Ethanol was found to be the ideal solvent for the reaction with the highest yield of 92% while polyethylene glycol was found to be the moderate one with a 65% yield. Dimethyl sulfoxide (DMSO) and Dimethylformamide (DMF) as solvents were also observed

Sr. no	Catalyst	Time (h)	Yield ^a
1.	No catalyst	10	ND ^b
2.	Et ₃ N	6	65
3.	Pyridine	6	68
4.	Potassium carbonate (K ₂ CO ₃)	6	80
5.	KOH	3	92
6.	Na ₂ CO ₃	6	25
7.	CH ₃ COONa	6	20

Table 2. Screening results of the base catalysts for 1,3,5 triaryl 2-pyrazoline at 40° C in ethanol as solvent. ^a Isolated yield. ^b Not determine.

Sr. no	Solvent	Time (h)	Temperature (°C)	Yield ^a (%)
1.	Neat	8	40	ND ^b
2.	THF	6	40	25
3.	PEG	6	40	65
4.	EtOH	3	40	92
5.	DMSO	7	100	70
6.	DMF	7	100	72
7.	DCM	9	40	ND
8.	Dioxane	8	100	ND

Table 3. Screening results of the solvents and temperature in Mannich reaction using KOH as a catalyst. Significant values are in bold. ^a Isolated yield. ^b Not determine.



Scheme 3. The condensation of -amino ketones and phenylhydrazine.

to facilitate this reaction (Table 3). Other solvents, including Dichloromethane (DCM) and dioxane were established to not promote the reaction.

With an optimized approach in hand, the scope of this process was then investigated using electron-rich and electron-deficient β -amino ketones. With all the examples, the corresponding 2-pyrazolines were formed in high yields (80–92%) (Scheme 3).

Following figure illustrates various KOH Base catalyzed 1,3,5-triphyenyl-2-pyrazoline by the condensation of -amino ketones and phenyl hydrazine.

After establishing the suitable condition for the synthesis of pyrazoline by the reaction of β -amino ketones with phenylhydrazine, derivatization was carried out using various substituted beta amino ketones. It was observed that, the electron withdrawing and electron donating groups like Cl, F, CH₃, Br, and OCH₃ in different rings have a marginal influence on the yields of the products as shown in Fig. 3.

Mechanism of the reaction

The presence of potassium hydroxide in ethanol may lead to the enhancement in the polarity of β -amino ketones. This increased polarity might result in greater reactivity towards phenylhydrazine. Since the carbonyl carbon is the only reactive centre available for nucleophilic addition, the addition of N1 to the carbonyl carbon might lead to the formation of the hydrazine product. Subsequently, the proton on N2 nitrogen may become available, generating an anion. This anion may facilitate the substitution of the aniline group, ultimately giving

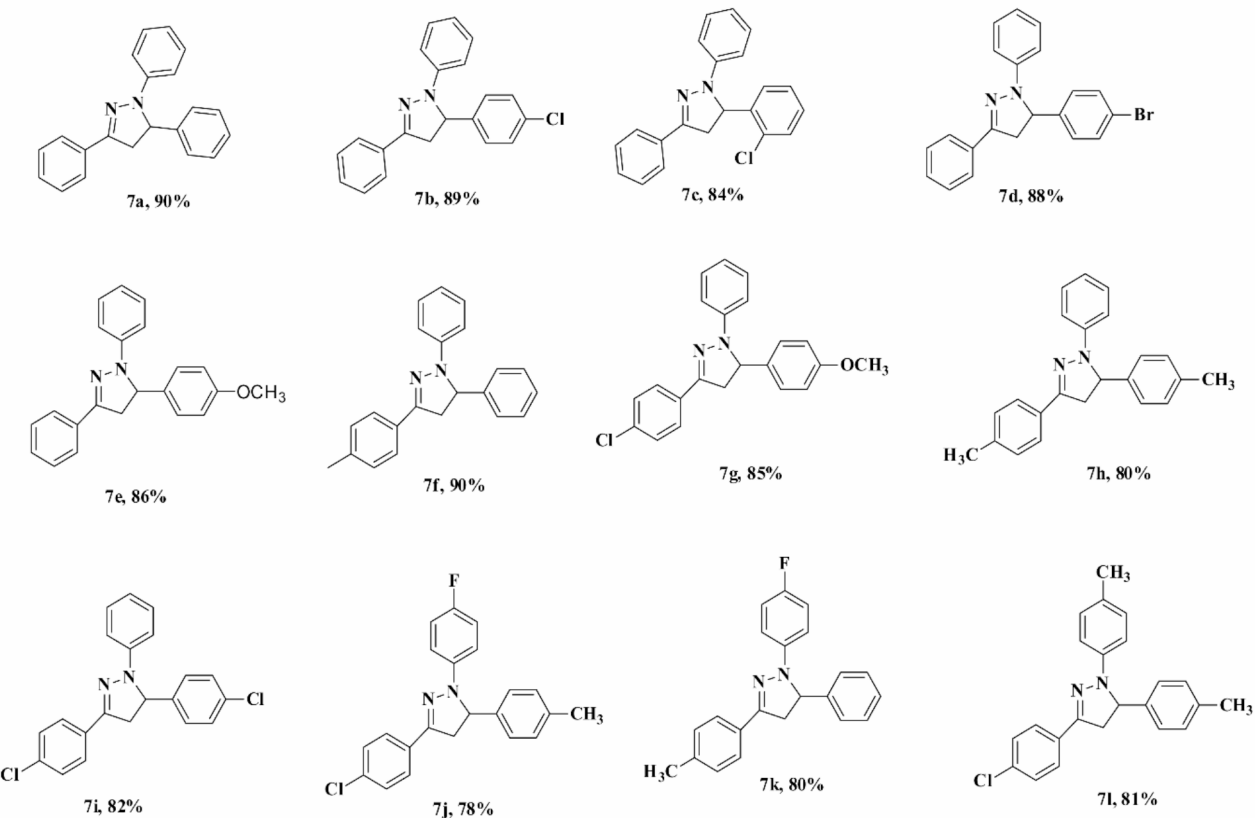


Fig. 3. Structures and yield of the compounds synthesized in this study.

rise to the formation of pyrazoline. It's important to note that this reaction proceeds cleanly and consistently yields products in the range of 80–92%, which strongly supports the mechanism illustrated in Fig. 4.

Characterization summary of the compounds

The structures of all products were confirmed by spectral means (IR, ^1H NMR, ^{13}C NMR, and GCMS) and by comparison with the literature data. In the IR spectra of synthesised pyrazolines, the stretching frequency at 1558 to 1575 cm^{-1} was assigned to $\text{C}=\text{N}$. A collection of medium bands was observed in the region 3028 to 2854 cm^{-1} that can be attributed to C-H stretching vibrations of the aromatic groups. These IR bands are supporting evidence for the formation of pyrazolines. In the ^1H NMR spectrum of pyrazolines, the doublet of a doublet at δ 3.18 with coupling constants $J=8$ Hz and 12 Hz was assigned to the Ha proton of C4. The doublet of a doublet at 3.88 ppm with coupling constants $J=8$ Hz and 12 Hz was assigned to the Hb proton of C4. Similarly, the doublet of a doublet at 5.31 ppm with coupling constants $J=8$ and 12 Hz was assigned to the Hc proton of C5. The aromatic protons appeared in the range of 7.11 to 7.72 ppm. In the ^{13}C NMR spectrum of pyrazolines, the signals appeared in the range of 111.77 to 146.52 ppm due to the aromatic carbons. The signal at downfield region 155.60 ppm was assigned to $\text{C}=\text{N}$ carbon. Two signals that appeared in the lower frequency region at 43.66 and 64.68 ppm were assigned to the methylene and methyl carbons at C4 and C5, respectively.

In silico study of the Triaryl-2-pyrazoline derivatives

The rationale behind target selection

In view of the recent Covid-19 pandemic, a lot of high throughput initiatives were undertaken in the hope to identify an effective anti-SARS-CoV-2 agent targeting the Mac1⁶⁷. One such fragment-based screening identified aryl pyrazoline as weak Mac1 inhibitor and was subsequently co-crystallized²¹. This fact demonstrates that aryl pyrazoline compounds indeed bind to the SARS-CoV-2 Mac1 with a limited strength. Based on this crystallographic evidence, here we attempt to extend the study by synthesizing the tri aryl derivatives of original pyrazoline fragment. We aim to check the possible application of newly synthesized Triaryl-2-pyrazoline derivatives as Mac1 inhibitors using in silico approaches.

Structural and functional anatomy of the identified target

The structure of the Mac1 consists of a very intricate collection of various functionally overlapping motifs. For example, Schuller et al. recently reported the presence of 5 functionally important locations on the Mac1 based on the interaction with the ADP-ribose molecule²¹. These include the adenine site (Asn20-Glu25, green), catalytic site (Val35-Ala56, cyan), a potential allosteric site (Gly85-Pro98, Yellow), ribose phosphate site (Pro125-Pro136,

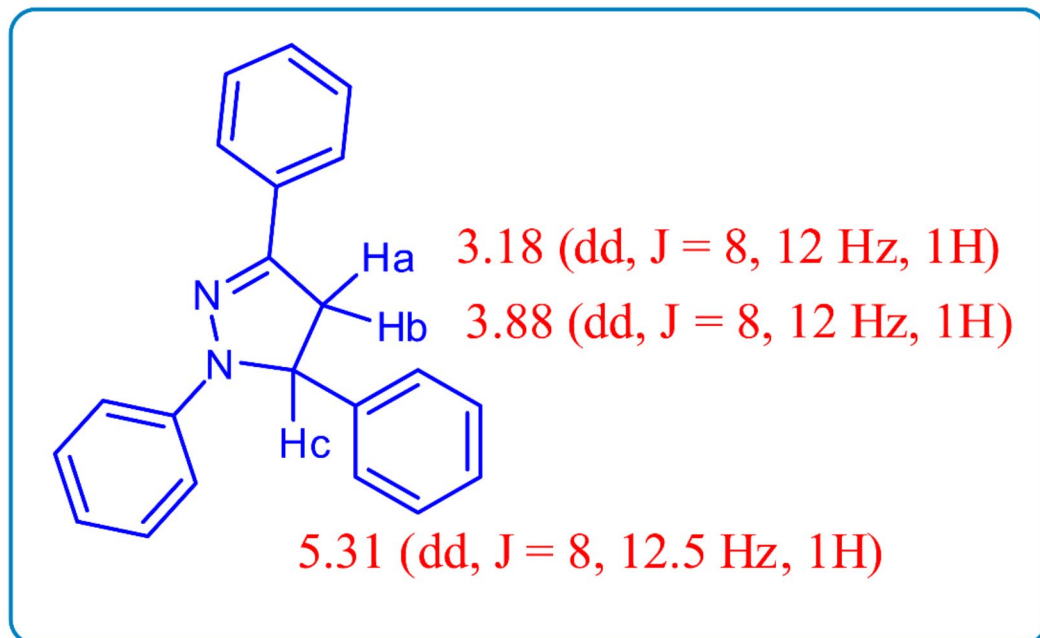
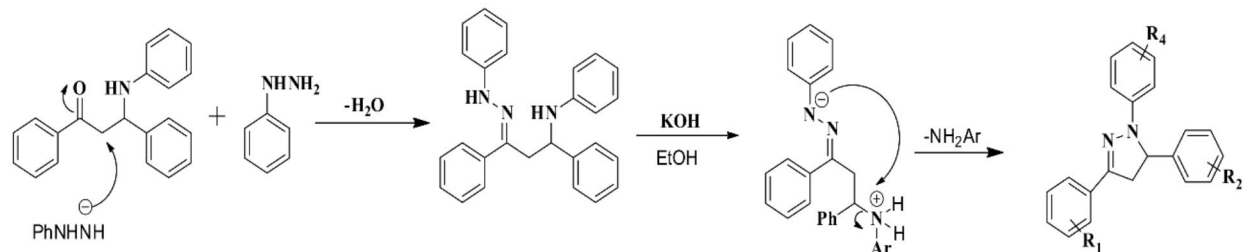


Fig. 4. Mechanism involving the proton chemical shift and coupling constant of compound 7a.

orange), and the adenosine site (Asn150-Leu160, red). All these sites are mapped onto the surface of the protein Fig. 5. The majority of the residues from the potential allosteric site appear to be buried in the core of the protein while the residues of the remaining sites are present on the surface. Additionally, the small two-residue motif formed by residues Phe156 and Asp157 is often referred to as the oxyanion subsite or oxyanion motif located inside the adenosine site. The catalytic site in turn is subdivided into three sub-sites, namely, the phosphate tunnel (placed on the protein where the diphosphate moiety of the ADP-ribose binds), followed by the ribose subsite (where the distal ribose fragment of the ADP-ribose attach) which leads to the outer subsite that is formed by Asn40 and Asn99. Asn40 is believed to be the major catalytic residue⁶⁸. Recently, the K-90 site was identified which constitutes the pocket surrounding the Lys90 residue and hence the name. The K-90 site appears to be a distinct location on the Mac1 on the opposite side of the active site. The residues lining the K-90 site includes Pro32, Thr33, Gly85, Ala89, Lys90, and His91 (Magenta). Many chemical fragments were observed to attach at this K-90 site. The functional significance of this site yet remains unexplored. Since most of the residues from the K-90 site overlaps with the allosteric binding site, the residues from this site can be assumed to play a role in the dynamic rearrangement of residues during allosteric interconversions. Another group alternatively termed the aforementioned location on the NSP3 domain as the adenine binding site (A), distal ribose binding site (R1), diphosphate-binding site (P1-P2), and the proximal ribose-binding site (R2)⁶⁹. To maintain consistency and avoid confusion, this report will follow the site convention adopted by Schuller et al.²¹.

Molecular docking

The results obtained from the virtual screening of the newly synthesized Triaryl-2-pyrazoline compounds are summarized in Table 4.

The summary of interaction demonstrates that the compounds present in the series of Triaryl-2-pyrazoline have enormous potential to interact with the Mac1 via effective nonpolar interactions. The following section attempt to explore such important non-polar interactions that newly synthesized compounds can putatively form with the Mac1. We also discuss the structural and functional significance of these non-polar interactions in the Mac1 inhibition in the subsequent sections.

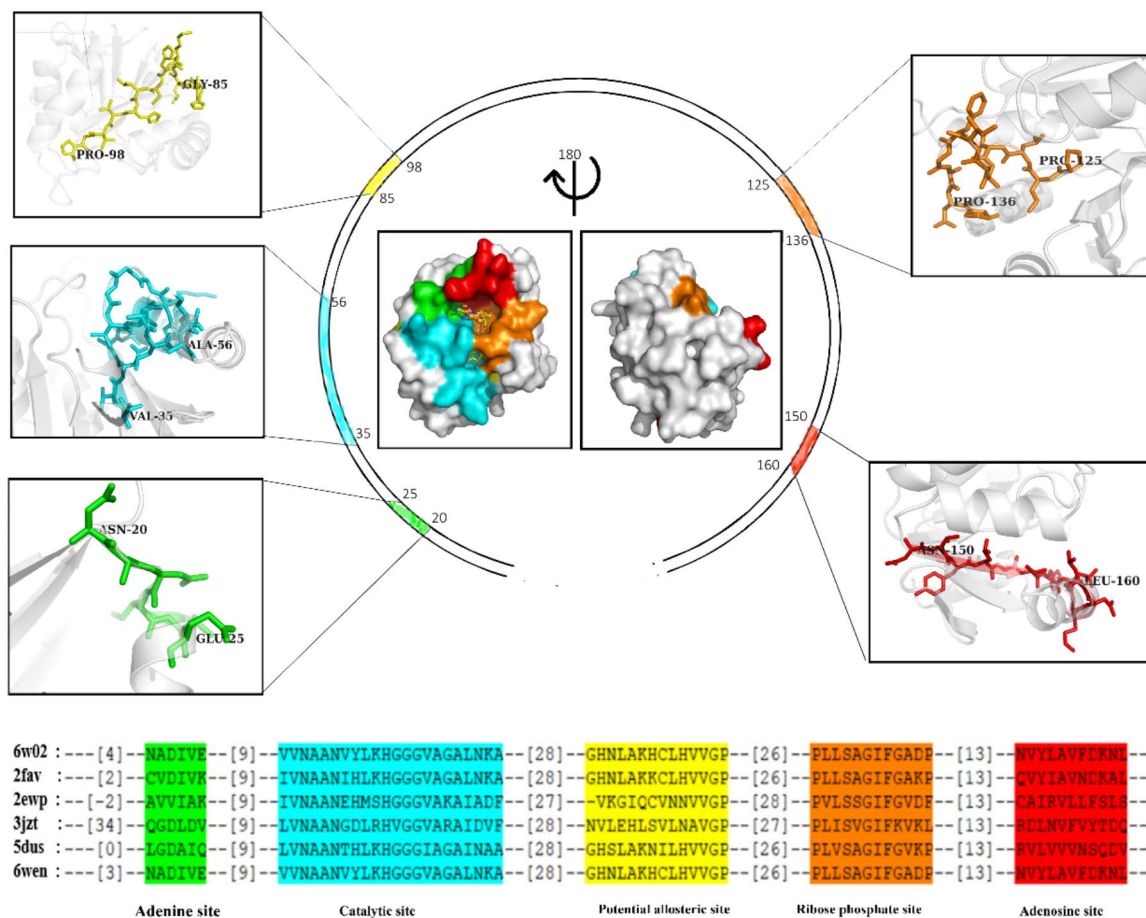


Fig. 5. Structural and Functional anatomy of NSP3 macro domain from SARS-CoV-2.

Structural inspection of the docking results demonstrates that the majority of compounds form an effective van der Waal's contact with residues like Pro125, Leu126, Gly133, Ala134, Asp135, Ala154, Phe156, and Asp157. Additionally, some compounds like 7b and, 7e form unique van der Waal's contact with the atoms from residues like Lys163 and Asn159 respectively.

Crystallographic studies conducted for comparing the Apo and the substrate-bound form of the Macrodomain indicate that a water-mediated contact between the atoms from ADP-ribose and the atoms from Leu126 and Ala154 is crucial for successful substrate binding⁶⁹. The same study also recognized that the distil ribose moiety of the substrate forms a water-mediated contact with the main chain amide group of Leu126 and Ala154. Ala154 is present in the adenosine site. Besides having a crucial role in ADP-ribose recognition, contact with this residue is also described as necessary for inhibition of the Mac1 using a variety of inhibitors including pyrroles, diaminopyridines, succinimides, thiazoles, amides, ureas, and pyrazoles class of compounds²¹. It is noteworthy from Table 4 that the predicted binding free energy values for all compounds falls within a very narrow range, ranging from -5.1 to -5.84 Kcal/mol. Moreover, the binding free energy of the reference crystallographic inhibitor was determined to be -4.46 Kcal/mol. Although AutoDock or AutoDock Vina is very well known for its excellent pose prediction capability, its scoring function is reported to have a standard error of 2.85 Kcal/mol when tested on 116 experimentally resolved protein-ligand complexes⁷⁰. Considering the binding free energy values obtained in a constant range in this study and the established standard error in free energy estimation in AutoDock, it is difficult to prioritize the best Mac1 inhibitor candidates at this stage. This fact inspired us to include advanced MD simulations based end point estimation to delineate and prioritize the best compounds. Therefore, we conducted MD simulations of all 12 ligands along with the crystallographic inhibitor in this study. Moreover, there were repulsive forces detected in the docking results (Table 4) due to very short interatomic distances between ligand and atoms from Gly130 residue. Considering the continuous dynamic state of the protein ligand system, it is highly unlikely for such repulsive forces to persist over an extended period. Therefore, another objective to perform MD simulation was to monitor if such repulsive forces detected between protein ligand complexes persist through out subsequent MD simulations.

MD simulation study

Results obtained from molecular docking consider ligand flexibility, while the protein molecule is usually considered rigid. However, in physiological conditions, both the entities (protein as well as ligands) are in

Compounds	Binding free energy (Kcal/mol)	Interaction details							
		van der Waal		Pi-sigma	Pi-anion	Pi-alkyl	Halogen-alkyl	Alkyl-alkyl	Repulsive force
7a	-5.1	Leu126, Gly133, Ala134, Asp135, Ala154, Phe156, Asp157	Leu160	-		Ala129, Pro136, Val155	-		Gly130
7b	-5.28	Gly133, Ala134, Asp135, Ala154, Phe156, Asp157, Lys163	Leu160	-		Leu126, Ala129, Pro136, Val155	-		Gly130
7c	-5.5	Pro125, Gly130, Gly133, Ala134, Asp135, Ala154, Phe156	-	Asp157		Leu126, Ala129, Pro136, Val155, Leu160	-		-
7d	-5.77	Leu126, Gly133, Ala134, Asp135, Ala154, Phe156, Asp157	-	-		Ala129, Pro136, Val155	Lys163		Gly130
7e	-5.44	Leu126, Gly133, Ala134, Asp135, Ala154, Phe156, Asp157, Asn159	Leu160	-		Ala129, Pro136, Val155	-		Gly130
7f	-5.25	Leu126, Gly133, Ala134, Asp135, Ala154, Phe156, Asp157	Leu160	-		Pro125, Ala129, Pro136, Val155	-		Gly130
7 g	-5.2	Pro125, Leu126, Gly130, Gly133, Ala134, Asp135, Phe156, Asp157, Lys163	Leu160	-		Ala129, Pro136, Val155	Ala154		--
7 h	-5.44	Leu126, Gly130, Gly133, Ala134, Asp135, Ala154, Phe156,		Asp157		Pro125, Ala129, Pro136, Val155, Leu160		Pro125, Val155, Leu160	
7 i	-5.84	Leu126, Gly133, Ala134, Asp135, Val155, Phe156, Asp157, Asn159, Lys163	Leu160	-		Ala129, Pro136	Pro125, Ala154, Leu160		Gly130
7j	-5.54	Leu126, Gly130, Ala134, Asp135, Phe156, Asp157,	Leu160			Ala129, Pro136, Val155	Gly133, Ala154	Lys163, Leu160	
7k	-5.21	Leu126, Ala134, Asp135, Ala154, Phe156, Asp157	Leu160			Ala129, Pro136, Val155, Leu160	Gly133	Pro125,	Gly130
7 L	-5.61	Pro125, Gly133, Ala134, Asp135, Phe156, Asp157	Leu160			Ala129, Pro136, Val155	Ala154	Lys163, Leu160	
Standard	-4.46	Gly133		Asp135		Pro136		Ile137, Lys163, Leu160	

Table 4. Summary of the interaction of triaryl-2-pyrazoline compounds with the Mac1 of SARS-CoV-2.

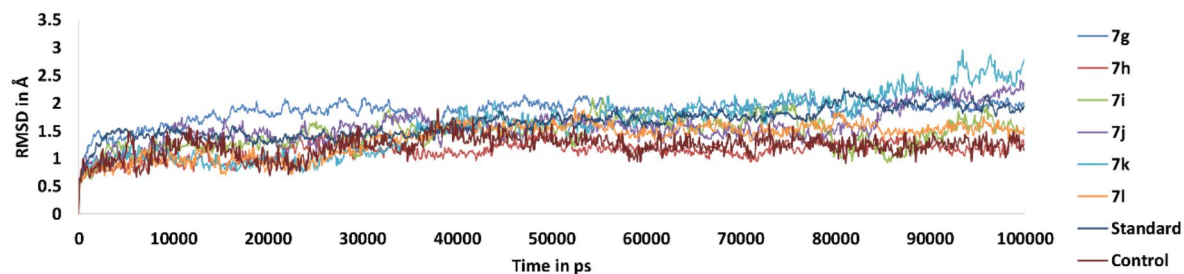
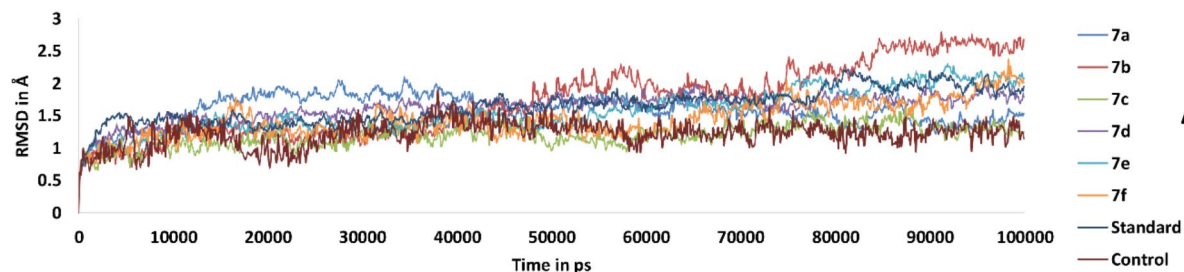
continuous dynamic states⁷¹. In such a dynamic state, numerous interactions are formed, and some interactions are disrupted simultaneously. Eventually, this dynamics governs the rate of enzyme catalysis as well as inhibition⁷². Such interactions are totally missed if relied solely on the results of molecular docking. It is to be noted that there are a lot of polar amino acid residues present in the binding pocket and the central pyrazoline core also offers nitrogen for effective polar interactions with these residues. However, no polar interactions (in the form of hydrogen bonds) are detected in the results obtained from molecular docking analysis (Table 4). Therefore, MD simulations were performed to monitor the possible role of hydrogen bonding in the stabilization of the pyrazoline inhibitor in the Mac1 binding site. Endpoint free energy estimation techniques like MMPBSA, MMGBSA and LIE offer relatively more accuracy in free energy estimation in comparison to any scoring function-based method⁶⁰. Therefore, to account for dynamic interactions and to increase confidence in free energy estimation, we conducted molecular dynamics simulations.

RMSD and RMSF analysis of trajectories

RMSD is an indicator of the conformational stability of the protein-ligand systems in MD simulations⁷³. RMSD is popularly used to detect if a protein-ligand system has converged toward an equilibrium state. A molecular system is assumed to be converged when RMSD acquires steady values and dramatic fluctuations are stopped. Typically, RMSD values in the range of 1–3 Å are tolerated along the plateau in the resulting RMSD plot and hence the system is said to have converged and conformational stability is assumed to be acquired. Figure 6A,B represents the time-dependent evolution of the protein-ligand trajectory for the time-lapse of 100 nanoseconds (ns). From the RMSD plots observed here, it can be inferred that most of the protein-ligand simulations converge around 1.5 Å RMSD. None of the RMSD values are observed to fluctuate drastically and hence the protein-ligand systems are assumed to obtain conformational stability.

An interesting structural pattern is to be noted in the RMSD results. In the control system, the protein demonstrates convergence at a lower RMSD value in comparison to the test ligands, indicating relative stability in the absence of ligands. This suggests a minimal deviation from the initial conformation during the simulation, hinting at the potential absence of significant conformational changes or fluctuations without ligand presence. Conversely, higher RMSD values observed for both hit candidates and the standard drug suggest that these compounds induce notable conformational changes or fluctuations in the protein structure upon binding. This observation implies a potential influence of ligands on the stability and dynamics of the protein conformation. Furthermore, the ligand-protein complexes (hit candidates and standard drug) exhibit higher RMSD values compared to the protein alone, indicating increased dynamic behaviour. This suggests that the complexes may introduce flexibility or prompt the protein to explore diverse conformational states.

RMSD



RMSF

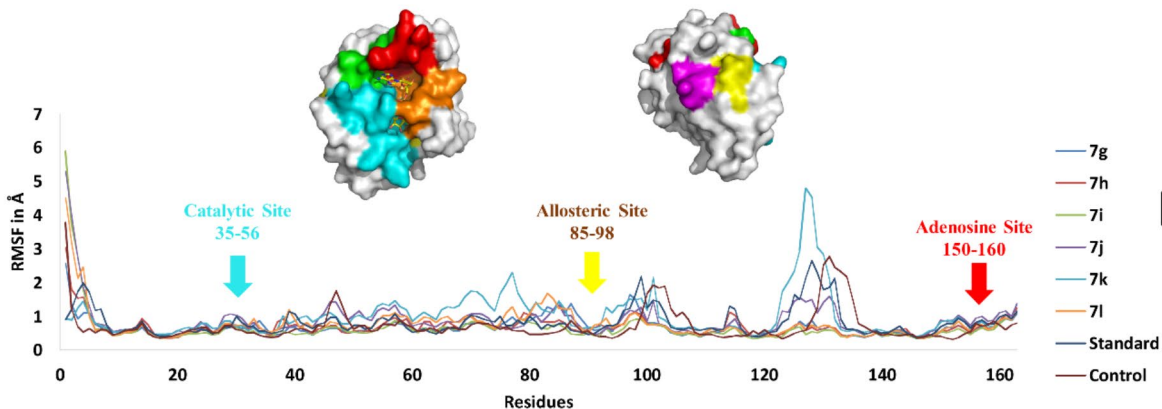
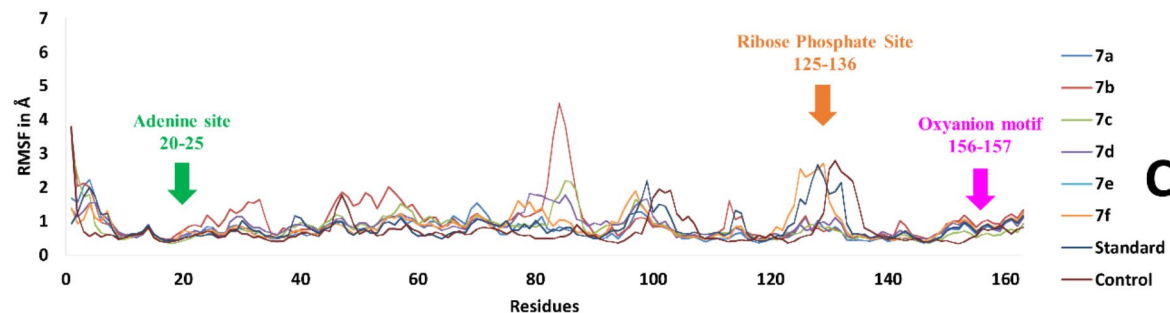


Fig. 6. The RMSD and RMSF plots of the protein ligand complexes.

RMSF is generally used to infer structural flexibility in the residues during the course of the simulation. Empirical studies suggest that lower RMSF values reflect the stability of the protein-ligand complexes⁷⁴. Careful inspection of the RMSF plot (Fig. 6C,D) indicates that the N-terminal region of the protein shows higher flexibility which can be attributed to the fact that the terminal regions are free and hence have a higher degree of flexibility. The core region of the protein where most of the catalysis and inhibition occurs (residues 35–56) is observed to have minimum fluctuation and thus can be considered stable. Interestingly, it is to be noted that in the case of compound 7b, high flexibility is observed in the potential allosteric site (Fig. 5). This

observation is conceptually concurrent with the fact that allosteric sites usually undergo a larger magnitude of spatial rearrangements. The ribose phosphate site is observed to have local fluctuations around the range of 2 to 5 Å indicating the rearrangement of residues in this region for adjustment of the aryl functional group from the ligand.

SASA analysis

SASA analysis was conducted to obtain insights into the changes in the accessible surface area of the ligand during the simulation. The results of SASA are summarized in Fig. 7A,B. It is clear that all the test ligands demonstrate the converged value of SASA around 6 nm². Convergence of SASA values is a reflection of the fact that the pyrazoline ligands have achieved a stable binding mode within the Mac1 binding site⁷⁵. The ligands thus may have found a conformation that maximizes its interaction with the surrounding residues, leading to a consistent SASA value, and may successfully form a stable complex with the viral Mac1⁷⁶. The convergence of SASA values of the standard ligand is observed to be around 3.5 nm² as compared to the test pyrazoline which converged around 6 nm². This differential convergence can be attributed to the fact that the crystallographic or standard ligand is a single aryl-substituted pyrazoline structure compared to the tri-aryl substituted test compounds in the present study. The additional two aryl substitution increased the overall surface area of the ligand and eventually SASA in the simulation.

Significant perturbation in the SASA profile may indicate alterations in the binding affinity or stability of the protein-ligand complex⁷⁷. The constant values of SASA observed in the current study are thus an indication of the formation of a stable protein-ligand complex in the MD simulation.

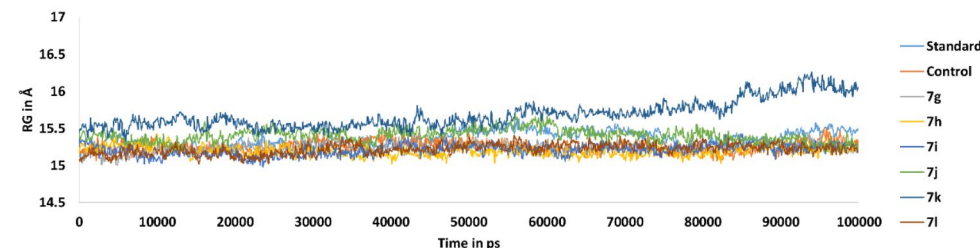
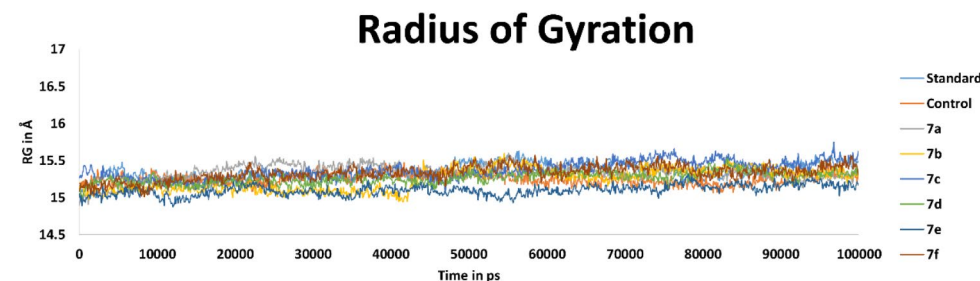
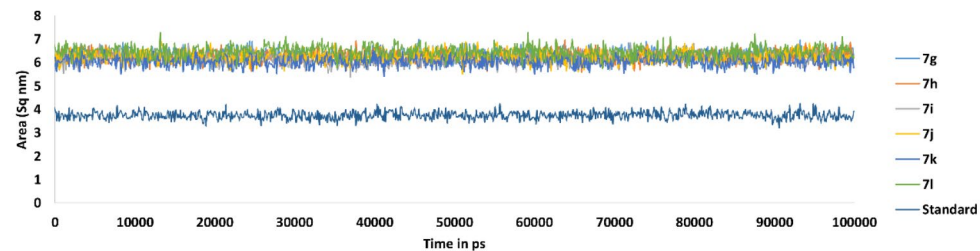
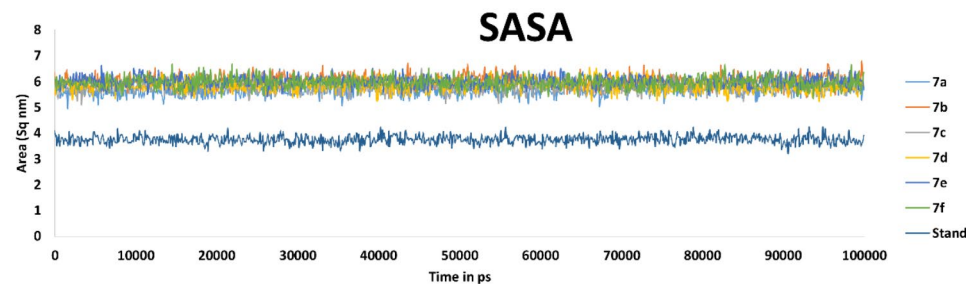


Fig. 7. The SASA plots of the ligand and RG plots of the protein ligand complexes.

RG analysis

The RG analysis in a protein-ligand complex was conducted across the course of the MD simulation to observe the overall compactness or expansion of the pyrazoline-Mac1 system. A converged RG value of around 15 Å was observed in almost all pyrazoline derivatives (Fig. 7C,D). This observation may suggest that the pyrazoline-Mac1 system has adopted a relatively compact conformation in the MD simulation. These results indicate attaining a stable and well-packed binding mode, where the protein-ligand system maintains a consistent overall size during the simulation. In case of 7k, there appears to be a slight perturbation of RG. But these perturbation are in very small scale (within 1 Å). The change in RG corresponds to the structural arrangement in amino acid residues to accommodate the methyl group from one hydrophobic pocket to another. The functional details of this rearrangement is discussed in the cluster analysis section.

Hydrogen bonding analysis

The trajectory analysis of hydrogen bonding interactions in the studied protein-ligand systems revealed distinctive patterns and occupancies for various ligands summarized in Table 5.

The frequency of hydrogen bonding observed in the trajectory is expressed as occupancy in hydrogen bonding analysis⁷⁸. Typically, this term measures the fraction of times when hydrogen bonds were observed in a trajectory⁷⁹. In this way, higher occupancy percentage reflects larger contribution of a hydrogen bond in the stabilization of the protein-ligand complex. Ligand 7c formed a prominent hydrogen bond with the side chain of Asp157, with an occupancy as high as 44.40%. Compounds 7d and 7e demonstrated hydrogen bonding interactions with main chain of Ala134, with respective occupancies of 25.20 and 23.00% indicating a potential role of this interaction in stabilizing the protein-inhibitor complex. Ligand 7j exhibited multiple hydrogen bonding partners, including Gly48, Gly130, Ile131, and Asn101, with occupancies ranging from 0.20 to 13.80%. Ligand 7k displayed interactions with Gly130 and Asp157, with occupancies of 0.40 and 1.90%, respectively, the smaller occupancy values are indicative of trivial role of hydrogen bonding in case of compound 7k. Ligand 7 L formed a subtle hydrogen bond with Asp157, with an occupancy of 0.10%. Notably, the standard ligand engaged in hydrogen bonding interactions with Asp135 and Lys163, with occupancies of 3.10 and 3.20%, respectively. These findings underscore the diverse and ligand-specific nature of hydrogen bonding interactions, providing valuable insights for understanding molecular recognition and ligand binding dynamics in the investigated system. Therefore, hydrogen bonding data from the MD simulations revealed the possibility of existence of polar interaction between the synthesized pyrazoline ligand and the conserved residues from the Mac1 binding site. The detailed discussion on the structural and functional roles of these residues is provided in the subsequent section.

Free energy estimation using end-point methods

Three end-point methods, namely MMPBSA, MMGBSA and LIE were utilized for free energy estimation from the MD simulation trajectories.

The free energy values for the protein-ligand complexes obtained by MMPBSA method are summarized in Table 6.

Compound 7 g is the only mono-substituted compound that showed comparable binding free energy value. The methoxy substituent in 7 g appears to impart stabilizing effect. Visual inspection of the trajectory revealed the fact that the complexes in which ligand was observed to be fixed firmly in the binding site (7a and 7b) have

Sr. no.	Ligand	Hydrogen Bonding Partner	Occupancy
1	7a	—	—
2	7b	ALA129-Main	5.50%
3	7c	ASP157-Side	44.40%
4	7d	GLY130-Main ALA134-Main	0.10% 25.20%
5	7e	GLY130-Main ALA134-Main GLY130-Main	0.30% 23.00% 0.50%
6	7f	—	—
7	7 g	—	—
8	7 h	—	—
9	7i	—	—
10	7j	GLY48-Main GLY130-Main ILE131-Main ASN101-Side	0.20% 13.80% 3.30% 0.10%
11	7k	GLY130-Main ASP157-Side	0.40% 1.90%
12	7 L	ASP157-Side	0.10%
13	Std	ASP135-Side LYS163-Side	3.10% 3.20%

Table 5. Summary of the hydrogen bonding analysis results.

Compounds	Δ Electrostatic interaction	Δ Van der Waal force	Δ Poisson Boltzmann	Δ Surface area	Δ Gas phase energies	Δ Solvation free energy	Δ Polar interactions	Δ Non polar interactions	Total free energy ΔG
7a	2.4 \pm 1.4	-22.3 \pm 1.4	17.4 \pm 2	-3.6 \pm 0.1	-24.7 \pm 2.1	13.8 \pm 2	15 \pm 1.7	-25.9 \pm 1.5	-10.9 \pm 1.6
7b	-4.1 \pm 1.9	-23.5 \pm 2.3	24.8 \pm 4.5	-4.2 \pm 0.2	-27.7 \pm 3.6	20.5 \pm 4.3	20.69 \pm 3.6	-27.8 \pm 2.5	-7.1 \pm 2.7
7c	-48.8 \pm 9.2	-13.7 \pm 2.6	61.5 \pm 8.9	-3 \pm 0.1	-62.6 \pm 8.6	58.4 \pm 8.9	12 \pm 4.5	-16.7 \pm 2.7	-4.1 \pm 3.8
7d	-7.3 \pm 2.1	-22.7 \pm 2.1	24.3 \pm 3.4	-3.5 \pm 0.1	-30.1 \pm 3.4	20.8 \pm 3.4	17 \pm 2.6	-26.37 \pm 2.1	-9.3 \pm 2.7
7e	-1.5 \pm 2.1	-11.9 \pm 2.9	12.9 \pm 6.5	-2.7 \pm 0.3	-13.4 \pm 4.4	10.1 \pm 6.3	11.4 \pm 5.6	-14.7 \pm 3.2	-3.3 \pm 4.3
7f	-0.9 \pm 2.1	-21.6 \pm 2.1	20.5 \pm 3.8	-3.9 \pm 0.2	-22.6 \pm 2.6	16.6 \pm 3.7	19.6 \pm 3.1	-25.6 \pm 2.3	-5.9 \pm 2.8
7g	-4.8 \pm 2.4	-24 \pm 2.3	24.8 \pm 3.9	-4.1 \pm 0.1	-28.8 \pm 4	20.7 \pm 3.8	19.9 \pm 2.6	-28.1 \pm 2.4	-8.1 \pm 2.1
7h	-1.2 \pm 1.8	-21.4 \pm 1.8	17.5 \pm 3.1	-3.8 \pm 0.1	-22.7 \pm 2.7	13.7 \pm 3	16.2 \pm 2.4	-25.2 \pm 2	-9.0 \pm 1.9
7i	-8 \pm 1.8	-23 \pm 1.6	23.8 \pm 3.2	-3.8 \pm 0.1	-31.1 \pm 2.2	19.9 \pm 3.1	15.7 \pm 2.5	-26.9 \pm 1.6	-11.1 \pm 2.1
7j	-1.7 \pm 3	-20.5 \pm 3.7	18 \pm 3.6	-3.4 \pm 0.4	-22.3 \pm 3.5	14.5 \pm 3.3	16.2 \pm 4.3	-24 \pm 4.2	-7.7 \pm 2.7
7k	2.0 \pm 1.5	-17.8 \pm 2.4	8.8 \pm 3.2	-3.5 \pm 0.3	-15.7 \pm 2.9	5.2 \pm 3	10.9 \pm 2.8	-21.4 \pm 2.6	-10.5 \pm 1.9
7L	-7.4 \pm 2	-28.4 \pm 1.7	27.2 \pm 4.2	-4.3 \pm 0.1	-35.8 \pm 2.6	22.9 \pm 4.2	19.7 \pm 3.4	-32.7 \pm 1.8	-12.9 \pm 3.4
Standard	-5.7 \pm 5.4	-7.1 \pm 1.9	12.8 \pm 7.5	-1.9 \pm 0.1	-12.9 \pm 5.8	10.9 \pm 7.4	7.1 \pm 4.6	-9.1 \pm 2.1	-2 \pm 4

Table 6. Summary of the MMPBSA free energy calculations. The data expressed above for different terms in MMPBSA free energy estimation was collected from the final 100 frames of the trajectory. Therefore, the values above are mean \pm sd for the last 100 frames. The numbers are limited to one decimal precision as reported in the log file obtained from the CaFE software. Standard ligand is the experimentally verified co-crystallized compound in the original PDB file. All values are in Kcal/mol.

Compounds	$\langle Vdw \rangle$ bound	$\langle Ele \rangle$ bound	$\langle Vdw \rangle$ free	$\langle Ele \rangle$ bound	$\langle Vdw \rangle$	$\langle Ele \rangle$	Total free energy ΔG^*
7a	-48.3 \pm 2.5	-32.9 \pm 4.5	-12.1 \pm 6.4	-8.4 \pm 7.6	-36.1	-24.5	-14.6
7b	-44.9 \pm 2.5	-29.7 \pm 4.9	-0.0043 \pm 0	0.0020 \pm 0	-44.9	-29.7	-17.9
7c	-34.6 \pm 3.3	-97.5 \pm 14.8	-28 \pm 3.4	-110.6 \pm 11.2	-6.5	13.1	3.1
7d	-42.3 \pm 2.6	-27 \pm 4.4	-5.9 \pm 1.9	-3.6 \pm 3.1	-36.4	-23.5	-14.3
7e	-45.4 \pm 3	-24.4 \pm 4	-35.6 \pm 2.8	-27.2 \pm 4.5	-9.7	2.7	-0.8
7f	-41.3 \pm 3	-38.3 \pm 6	-11.6 \pm 2.8	-11.7 \pm 5.4	-29.7	-26.6	-14.1
7g	-45.1 \pm 3	-27.8 \pm 5.1	-4.2 \pm 1.8	-3.6 \pm 3.2	-40.8	-24.1	-15.3
7h	-39.8 \pm 3.2	-25.9 \pm 5	-18.3 \pm 4.6	-23.6 \pm 9.5	-21.5	-2.6	-4.7
7i	-38.7 \pm 3.7	-28.5 \pm 5.3	-1.05 \pm 0.6	-0.6 \pm 1.4	-37.7	-27.8	-15.9
7j	-45.07 \pm 3.4	-25.3 \pm 4	-19.2 \pm 3.5	-14 \pm 5.7	-25.8	-11.3	-8.3
7k	-41 \pm 2.6	-27.7 \pm 4.7	-0.9 \pm 1	-0.08 \pm 0.5	-40.11	-27.6	-16.3
7L	-42 \pm 2.8	-36.4 \pm 4.7	-0.01 \pm 0.003	0.02 \pm 0.1	-42.05	-36.46	-19.6
Standard	-0.3 \pm 0.9	-0.2 \pm 0.7	-11.3 \pm 2.9	-19.5 \pm 6.7	11	19	8.3

Table 7. Summary of the LIE free energy calculations. * The free energy obtained by using the standard empirical parameters $\alpha=0.18$, $\beta=0.33$ $\gamma=0$. The data expressed above for different terms in MMPBSA free energy estimation was collected from the final 100 frames of the trajectory. Therefore, the values above are mean \pm sd for the last 100 frames. The numbers are limited to one decimal precision as reported in the log file obtained from the CaFE software. Standard ligand is the experimentally verified co-crystallized compound in the original PDB file. All values are in Kcal/mol.

relatively lower binding free energy as compared to ligands that somehow moved towards the surface of the protein during the simulation (standard and 7c). This can be indicative that ligands bound at the core of the site are more energetically stable as compared to the ones that shifted towards the surface of the protein. Thus deep binding may impart stability to the Mac1-Ligand complex as compared to shallow binding at the surface of the protein.

The free energy values for the protein-ligand complexes obtained by LIE method are summarized in Table 7.

As per the LIE model, compounds 7a, 7b, 7d, 7g, 7i, 7k, and 7L seem to be potentially good binders owing to their recorded free energy values. Interestingly, compound 7g was revealed to possess better binding free energy in the LIE model (-15.3 Kcal/mol) as compared to MMPBSA calculations (-8.1 Kcal/mol). This observation thus supports to use of multiple free energy estimation methods for evaluating the compounds. Except, for compound 7g, the binding free energies obtained by both the endpoint methods are in accordance with each other. For example, compounds 7a, 7d, 7i, 7k, and 7L were observed to possess better binding free energy in LIE as well as the MMPBSA method. Similarly, compounds like 7c and 7e both achieved higher binding free energy. The differences in the magnitude of free energy values obtained by MMPBSA and LIE can be attributed to the

fact that LIE relies only on van der Waal's and electrostatic contribution and do not account for PB and SA terms. Hence in our study, LIE appears to over predict the binding energies as compared to the MMPSA method. Therefore, based on binding free energy values, compounds 7a, 7d, 7 g, 7i, 7k, and 7 L can be considered as better binders toward viral Mac1 since they have consistently demonstrated favourable binding affinity values in two independent endpoint estimation methods. At the same time, compounds 7c and 7e might not be a good choice for further investigation as they showed adverse values for affinity towards viral Mac1.

A comprehensive summary of the binding free energies for each ligand-protein complex via MMGBSA method is presented in Table 8.

The binding free energy results obtained from the MMGBSA method underlines a prominent trend. The free energy values obtained in MMGBSA analysis for all compounds in this study are constantly more negative than the respective MMPSA estimates. The more negative free energy values obtained from the MMGBSA is an indicative that the compounds are estimated to possess stronger binding interactions as compared to the MMPSA method. For example, in case of compound 7a, the binding free energy of -45.81 kcal/mol was estimated using MMGBSA method, whereas, MMPSA estimated -10.9 kcal/mol. This trend can be consistently observed across the remaining compounds, with MMGBSA demonstrating higher negative values, for instance -39.12 kcal/mol for compound 7 h (compared to -9.0 kcal/mol in MMPSA) and -42.90 kcal/mol for compound 7 L (compared to -12.9 kcal/mol in MMPSA).

The variance between MMGBSA and MMPSA can be attributed to the differences in the treatment of solvation effects by the two methods⁸⁰. MGBSA often predicts larger absolute binding free energies because of its implicit solvent model, which can better capture polar and nonpolar solvation effects⁸¹. In contrast, MMPSA, while valuable for general trends, tends to provide less extreme binding energy values and can sometimes underestimate interactions that are better represented by the generalized Born solvation model in MMGBSA^{82,83}. Overall, in the present study, the MMGBSA appears to provide a more conservative and more realistic estimates of the binding interactions for the set of compounds under consideration.

Cluster and interaction analysis of the selected compounds

Due to space constrain, in the following section we discuss the detailed structural and functional dynamics aspects of the protein-ligand complexes of the compound that recorded the best free energy values in the MMPSA and MMGBSA analysis. The detailed structural and dynamic description of the remaining compounds can be obtained in the supplementary material. Various interactions involving the Pi cloud, including Pi-Pi, Pi-Pi T-shaped interaction, Pi-sigma interactions, amide-pi stacked interaction, Pi-Anion interaction, etc., were observed in the current study. The general threshold for such Pi interactions is reported to range between 4 and 7 angstroms⁸⁴.

Compound 7a

In the docking results, the aryl rings of compound 7a were observed to be in pi-alkyl interaction with residues like Val155, Ala129, and Pro136 (Fig. 8). Residue Leu160 appeared to contribute pi-sigma interaction with the compound. However, during the course of the simulation, the pi-alkyl interaction with residues Val155, and Ala129 remained stable and the interaction with Pro136 appeared to be unstable as it is not detected in the cluster analysis results. Tracing the general distance of the pi-sigma interaction between atoms of compound 7a and Leu160 revealed that this contact was barely maintained at the distance of about 4 Å for initial 20 ns (Fig. 8). After 20 ns, the participating phenyl ring from the compound seems to reorient away from the general direction of Leu160 and hence this pi-alkyl interaction was destabilized for the remaining course of the simulation. Similarly, during the MD simulation, a very stable Pi-Pi T-shaped interaction was observed to be established between the phenyl ring of compound 7a and the phenyl ring of residue Phe156 after 30 ns that remained stable throughout the simulation. Therefore, based on the above-mentioned fact, it can be concluded that Pi-Pi T-shaped interaction provided by Phe156 can stabilize the Mac1-7a complex more effectively as compared to the pi-sigma interaction made with Leu160.

Compounds	ΔG Bind covalent	ΔG Bind lipo	ΔG Bind Solv GB	ΔG Bind VdW	Ligand strain energy	ΔG bind
7a	3.0	-22.11	15.42	-37.38	4.16	-45.81
7b	8.1	-21.80	-6.40	-29.27	12.03	-28.09
7c	0.04	-5.87	7.27	-18.84	0.43	-20.81
7d	1.35	-12.89	-0.21	-27.95	1.53	-37.96
7e	5.84	-12.98	3.33	-28.54	6.29	-32.52
7f	1.82	-19.07	-10.18	-27.43	4.22	-35.44
7 g	6.37	-17.98	-11.96	-27.03	5.51	-30.30
7 h	3.20	-19.86	-10.70	-34.11	3.65	-39.12
7i	-0.23	-14.44	-2.46	-29.05	1.60	-30.81
7j	3.50	-18.01	-0.86	-31.62	4.43	-39.06
7k	1.46	-17.11	-5.00	-32.54	2.94	-37.91
7 L	0.73	-15.61	-4.89	-33.58	0.94	-42.90
Standard	0.53	-10.49	-3.512	-21.29	1.09	-31.49

Table 8. Summary of the MMGBSA free energy estimation.

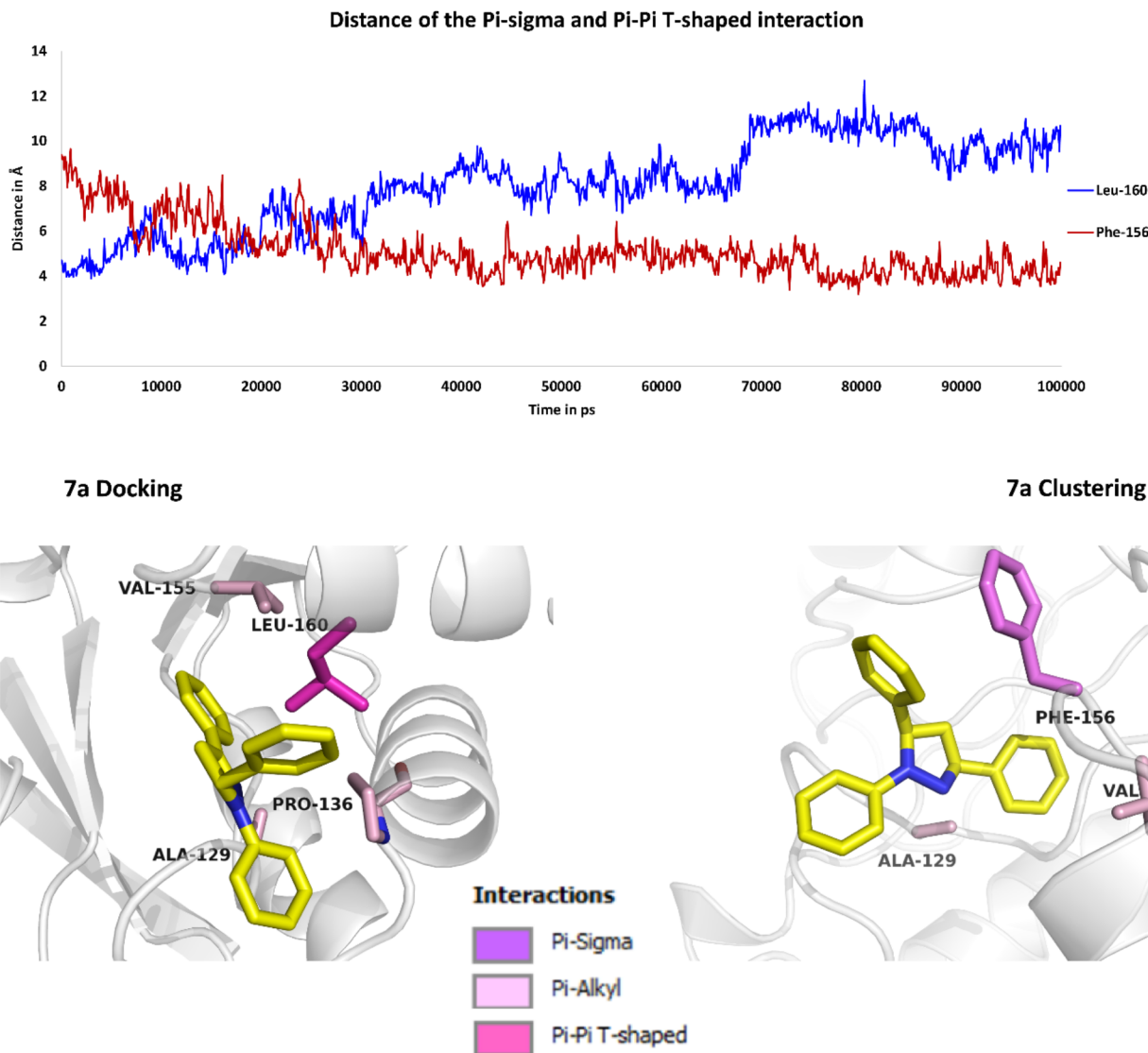


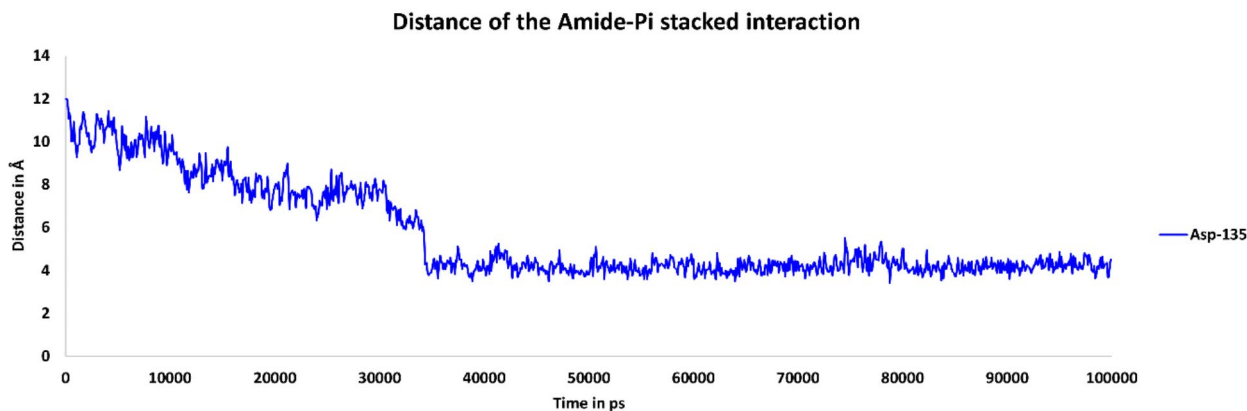
Fig. 8. Interaction analysis of compound 7a with residues from Mac1. Distance plot of pi-sigma interaction between compound 7a and Leu160 (Blue) and Pi-Pi T-shaped interaction with residue Phe156. Comparison of interactions obtained from docking results and cluster analysis.

Compound 7d

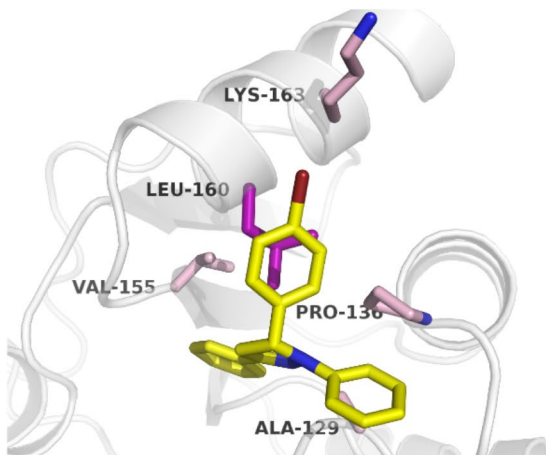
This compound was predicted to be stabilized by two pi-sigma interactions with residue Leu160 in the docking results. However, these interactions appeared to be transient and were not maintained intact through the MD simulation due to the dynamic rearrangement of the participating phenyl rings during the simulation. Interestingly, an amide-pi stacked interaction with residue Asp135 emerged during the cluster analysis of the MD simulation trajectory. Tracing the distance of this newly evolving interaction with Asp135, it became evident that this interaction was established around 34 nanoseconds and remained stable throughout the rest of the simulation trajectory (Fig. 9). Amide-pi stacked interactions are generally formed when the amide moieties from the protein main chain come in stacking contact with the pi surface from the ligands⁸⁵. Such amide-pi stacked interactions are already established to play a crucial role in the inhibition of serine protease factor Xa by various synthetic inhibitors^{86,87}. Therefore, amide-pi stacked interaction can potentially confer stability to compound 7d if it is tested for inhibition against the viral Mac1.

Compound 7 h

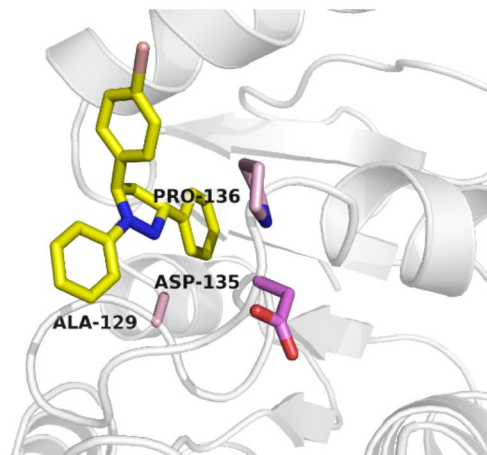
Compound 7 h is a dimethyl-substituted derivative of the triaryl pyrazoline scaffold. The docking studies predicted that the hydrophobic pocket formed of residues Val155, Ala129, Pro125, Leu126, Ala154, and Phe156 may act as an anchor to hold fast compound 7 h via one of its methyl groups. The other methyl group was oriented toward the outer boundary of the pocket supported by non-polar residues like Ala134 and Leu160



7d Docking



7d Clustering



Interactions

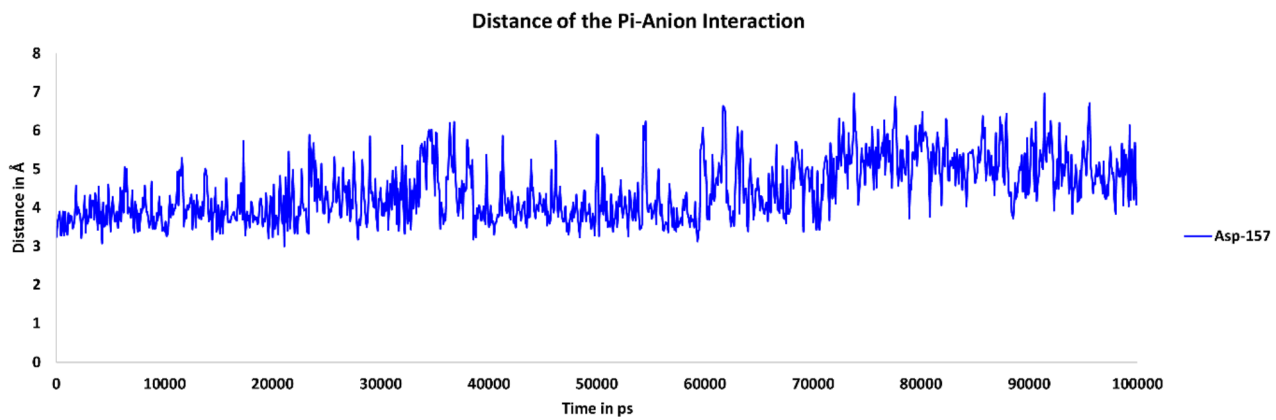
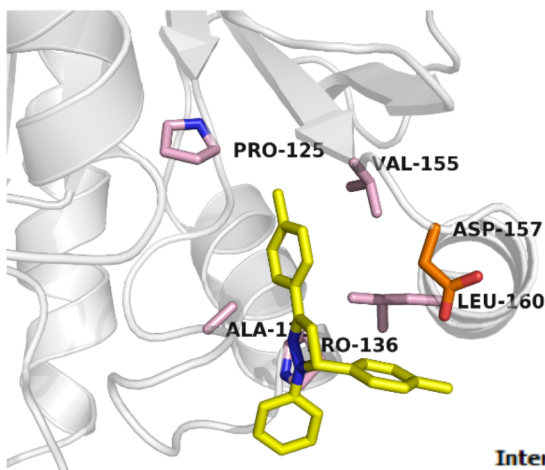
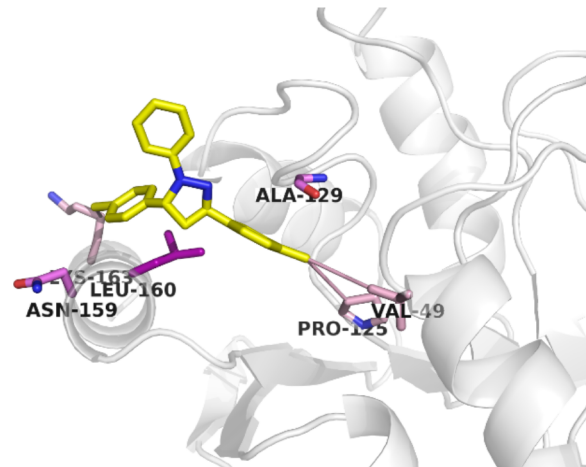
	van der Waals
	Amide-Pi Stacked
	Pi-Sigma
	Alkyl
	Pi-Alkyl

Fig. 9. Interaction analysis of compound 7d with residues from Mac1. Distance plot of amide-pi stacked interaction between compound 7d and residue Asp135. Comparison of interactions obtained from docking results and cluster analysis.

(Fig. 10). Interestingly, the side chain of Asp157 was observed to be at a distance of 3.2 Å from the aryl ring of compound 7 h thereby possibly involved in an effective Pi-Anion interaction. Pi-anion interactions are defined as non-covalent attractive forces that exist between aromatic systems that are electron deficient and anions⁸⁸. Pi-anion interactions are already known to play a pivotal role in molecular recognition⁸⁹. Wang and Wang demonstrated that Pi-Anion interactions are active and functional when the distance of the participating anion and pi ring is around 3 Å⁹⁰. This interaction was not observed in the representative pose obtained in the cluster analysis of the trajectory. However, tracing the distance of this interaction in the trajectory revealed that this Pi anion interaction was observed in 36% of the total simulation time and thereby, the role of this interaction in the stabilization of 7 h in viral Mac1 cannot be completely ruled out. The distance plot clearly demonstrates that in most of the simulation time, the distance between the pi system and the anionic atom of Asp157 was found to be stabilized between 3 and 4 Å. The visual inspection of the trajectory and the data obtained from cluster analysis is in line with the docking observation that the methyl group is indeed stabilized in a hydrophobic pocket formed by residues Leu126, Gly130, Val49, and Pro125.

Compound 7i

Compound 7i is a dichloro derivative of the parent triaryl pyrazoline chemical framework. The docking study detected a halogen bonding interaction between one of the substituted chlorine and the backbone carbonyl

**7h Docking****7h Clustering****Interactions**

█	van der Waals
█	Pi-Sigma
█	Amide-Pi Stacked
█	Pi-Anion
█	Alkyl
█	Pi-Alkyl

Fig. 10. Interaction analysis of compound 7 h with residues from NSP3-microdomain. Distance plot of pi-anion interaction with Asp157 and compound 7 g. Comparison of interactions obtained from docking results and cluster analysis are shown in the lower pane.

oxygen of Ala154. From a biomolecular interaction perspective, the halogen bonds are reported to impart stabilizing effect if the partner atoms are in the range of 3.5 Å distance⁹¹. The same study reported that the halogen bond formed by chloro, bromo, and iodo atoms are found to be in the general distance of 3.27, 3.37, and 3.5 Å respectively. The distance plot of this halogen bond clearly demonstrates that the distance converged around 6 Å in the MD simulation, which is out of the limit of the aforementioned halogen bonding distance (Fig. 11). Therefore, such halogen bonds are least likely to stabilize compound 7i in the viral Mac1. However, the results of cluster analysis reported an amide-pi stacking interaction with the main chain carbonyl oxygen atom of residue Ala129 to stabilize the 7i-Mac1 complex.

Compound 7k

Compound 7k is another di-substituted derivative of the triphenyl pyrazoline base compound. It has chloro and methyl groups substituted on two distinct phenyl rings. Elementary docking analysis predicted that this compound might be stabilized by the halogen bond of the substituted chloro group with residue Gly133. The aliphatic methyl group was suspected to be supported by Ala21, Asp22, Ile23, Pro125, Ala129, and Val155 residues that form an effective non-polar pocket. Cluster analysis results of MD simulation trajectories support the fact that the halogen bond with Gly133 might be transitory and might not play a role in stabilization. To confirm this observation, we traced the distance of this bond in the trajectory and observed that the halogen

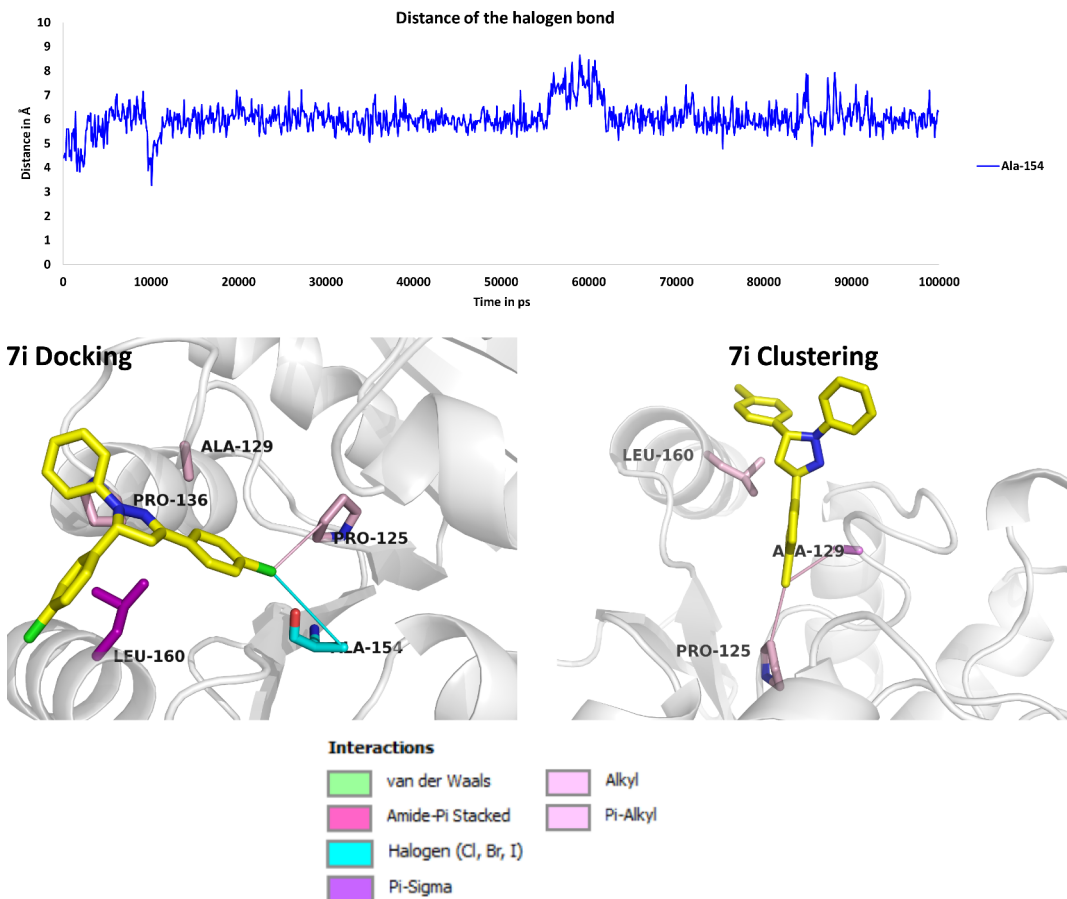


Fig. 11. Interaction analysis of compound 7i with residues from NSP3-microdomain. Distance plot of halogen bonding interaction with Ala154 and compound 7i. Comparison of interactions obtained from docking results and cluster analysis are shown in the lower panel.

bond was indeed very transient (Fig. 12) as it remained intact for the very first few frames in the trajectory. On the other hand, the methyl group showed interesting functional dynamics in this simulation. As mentioned above, this methyl group was predicted to be stabilized in a hydrophobic pocket formed by residues Ala129, Val155, and Pro125. However, with progression in time, the ligand evolved its orientation by shifting the methyl group to an entirely different hydrophobic pocket lined by residues Val36, Ala38, Val95, Pro125, Leu127 located at the distance of 8.5 Å of the initial hydrophobic pocket (Fig. 12). Therefore, such functional dynamics can help gain insights into understanding the inhibition process of this protein at finer resolutions.

Compound 7 L

Compound 7 L is a tri-substituted product in the present series that has two methyl groups and a single chloro group. This compound has been predicted to possess the most favouring binding affinity towards the viral Mac1 protein in both MMPBSA as well as LIE methods. This fact can be partially attributed to its ability to interact with various amino acid residues through its three separate functional groups. For example, docking and MD studies predicted that this compound can be stabilized by attractive forces like van der Waal's contacts, alkyl and pi-alkyl interactions, halogen bonds, pi-sigma contacts, and amide-pi stacked interactions. Notably, the halogen bond with Ala154 was not predicted in the cluster analysis results, but the distance-based analysis of this halogen bond indicates otherwise. The distance value for this halogen bond was found to converge around 3.5 Å length during the course of the simulation (Fig. 13). This observation clearly demonstrates a possibly crucial role in the stabilization of this compound in the Mac1. Halogen bonds are chemically defined as an attractive force that exists between the electrophilic portion of the halogen atom and the nucleophilic region of the partner chemical species⁹². The crystallographic studies carried out on compounds like IDD594 and Statil targeting aldose reductase enzyme established a decisive role of halogen bonds in not only recognition, but also binding the drugs to the enzyme and therefore overall inhibition process^{93–95}. In contrast, the amide-pi stacked interactions with Gly47 that were detected to exist in cluster analysis turns out to be unstable and remained intact for the transient time in the simulation.

Careful comparison of various 2D interaction plots (See supplementary material) reveals the fact that in many compounds, docking results predicted pi-Sigma stacking with Leu160, however, it was not observed to be consistent in the MD simulation. It is established that due to its charge transfer ability, pi-sigma interaction

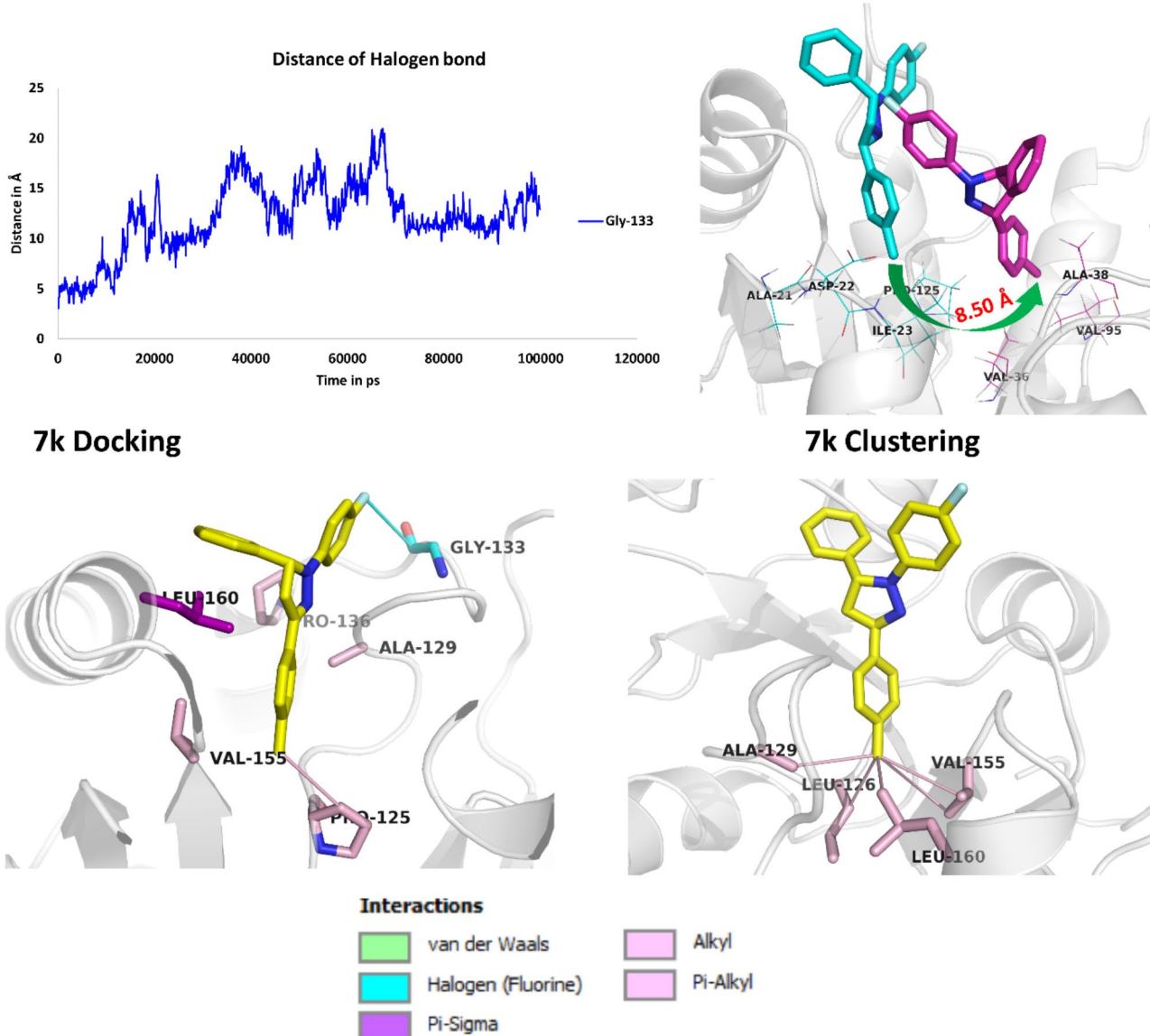
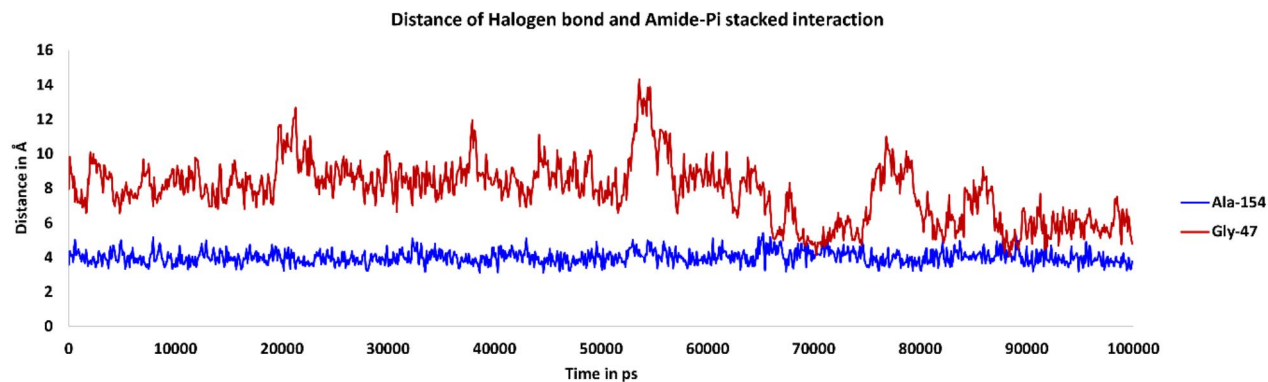


Fig. 12. Interaction analysis of compound 7k with residues from NSP3-microdomain. Distance plot of halogen bonding interaction with Gly133 and compound 7k (upper left). Illustration showing displacement of the methyl group into a new hydrophobic pocket (upper right). Comparison of interactions obtained from docking results and cluster analysis (lower).

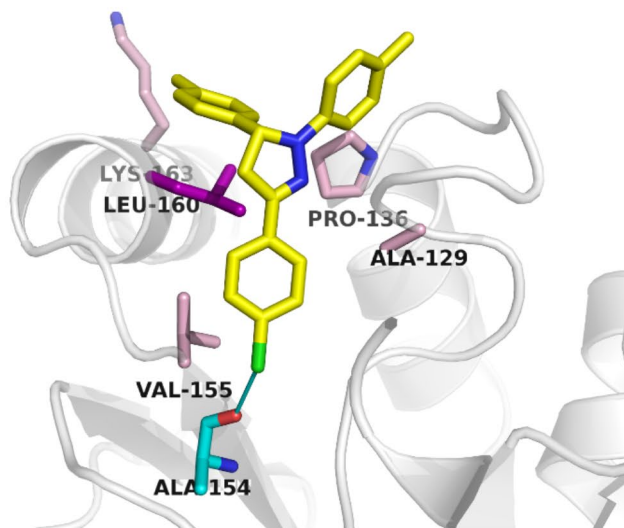
plays a decisive role in assisting the drug molecules to successfully intercalate in the binding site of the protein receptor⁹⁶. But based on the observations from the current study, a minor role of pi-Sigma stacking interaction with Leu160 can be assumed in the stabilization of the compounds.

In the current investigation, we made an attempt to correlate the thermodynamic stability of the Mac1-ligand complexes (accessed by the MMPBSA and MMGBSA binding free energy calculations) with the structural interaction analysis for compounds 7a, 7d, 7 h, 7i, 7k, and 7 L. The following discussion reveals that the thermodynamic stability was indeed complementary to the structural inspection.

One of the most prominent trend we observed in this study is the consistent more negative binding free energies across all compounds by the MMGBSA method, thereby signifying a stronger binding affinity and thus indicate a significant stabilizing effect of the pyrazoline ligands in the Mac-1 binding pocket. For instance, in case of compound 7a, the lower MMGBSA value as compared to MMPBSA (-45.81 and -10.9 ± 1.6 kcal/mol respectively) may reflect the significance of electrostatic and nonpolar interactions. This inclination perfectly corroborate with the MD observation where stable Pi-Pi and Pi-alkyl interactions were consistently maintained with residues like Ala129, Val155, and Phe156; whereas, pi-sigma interaction with residue Leu160 were observed to be transient. These structural dynamics my potentially contribute to the variance in the binding free energy estimation between the two methods.



7I Docking



Interactions

van der Waals	Alkyl	Halogen (Cl, Br, I)
Amide-Pi Stacked	Pi-Alkyl	Pi-Sigma

7I Clustering

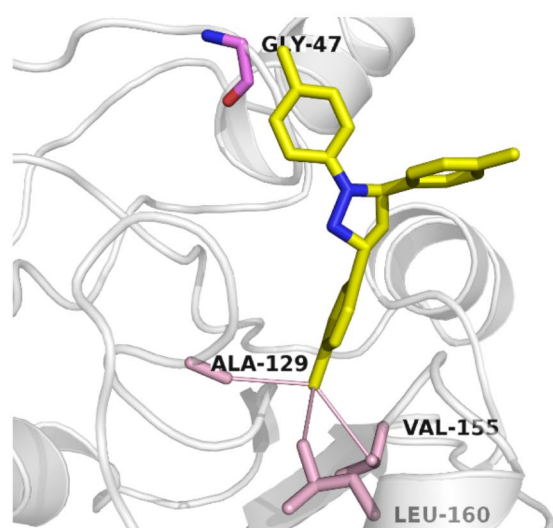


Fig. 13. Interaction analysis of compound 7 L with residues from NSP3-microdomain. Distance plot of halogen bond and amide-pi stacked interaction with Ala154 and Gly47 respectively with compound 7 L (upper). Comparison of interactions obtained from docking results and cluster analysis (lower).

Likewise, in the case of compound 7d, the MMGBSA computations estimated high stability (with -37.96 kcal/mol binding free energy value). This value supports the structural observation of Asp135 forming the amide-pi stacking interaction with the compound 7d. Interestingly, such amide-pi stacking interaction were experimentally testified to play a critical role in binding and inhibition in similar protein complexes⁸⁵. In case of compounds like 7 h and 7 L, the MMGBSA analysis recorded enhanced stability values (-39.12 and -42.90 kcal/mol, respectively). These high values can be attributed to the hydrophobic and Pi-anion interactions with residues like Asp157 along with the stable and consistent hydrogen bonding of 7i's with the backbone atoms of Ala154. These strong interactions revealed in the MD simulations are aligned with the negative binding free energy values, and therefore imply a thermodynamically favourable configuration.

The thermodynamic stability data regarding compound 7i and 7k obtained by MMGBSA method offers an explanation of the transitory nature of halogen interactions. For example, the structural data offered in this study during docking detected the halogen bonding interactions with Ala154 and Gly133, but they were observed to destabilize during the course of MD simulation. This fact correlates with the slightly less negative binding energies in MMPBSA thereby imitating their momentary stabilization role. On the other hand, the MMGBSA data highpoints the central role of consistent amide-pi stacking and lipophilic interactions with residue Ala129 that might contribute in imparting stability in absence of stable halogen bonds.

In a nutshell, the MMPBSA and MMGBSA analyses collectively reinforce the role of specific, stable interactions, such as Pi-Pi T-shaped and amide-pi stacked interactions, as primary contributors to binding stability in the Mac1-ligand complexes. The more negative MMGBSA energies further validate these key

interactions, providing a comprehensive thermodynamic basis to support the stabilization mechanisms proposed in the structural analysis.

Role of conserved residues: a comparative account of the established inhibitors of Mac1

Careful observation of docking poses as well as data from cluster analysis identified Pi-Sigma interaction of Phe156 with various compounds in the present series (see supplementary information). Phe156 occupies a very critical location in the active site of the Mac1 by providing an aromatic support in the adenine binding pocket⁹⁷. Sequence alignment data from various studies has observed this position to be very uniquely conserved across the species^{69,98,99}. Interaction with this residue is suspected to play a key role in engaging host cell contact⁹⁷. Evolutionary trace analysis conducted on the active site residues of Mac1 and related proteins supported the idea that novel chemical scaffolds can have greater selectivity if they are engaged in an interaction with this residue. Crystallographic studies have revealed that the aromatic contact of inhibitors like PARG-329 holds a key role in stabilizing it in the Mac1 active site⁹⁷.

Similarly, interaction with Ala129 confers unique functional significance. Crystallographic data demonstrates that loop containing Ala129 contributes in providing higher flexibility to the phosphate binding region. Dynamics in this loop is known to be crucial in the catalytic activity of viral Mac1. Mutagenesis studies carried out on the residues of this region indicates drastic reduction of enzymatic activity¹⁰⁰. Conformational alterations associated with Ala129 have been identified within the phosphate binding loop when Mac1 is bound to ADP-ribose²¹. The rearranged confirmation of this loop is generally referred to as the everted conformation. Compound like LL114_0041 is known to interact with Ala129 main chain and compound LL123_0020 seems to impart water mediated stabilization in the phosphate binding loop¹⁰¹. Similar water mediated stabilization of the phosphate binding region in Mac1 was also observed in case of experimental drug Z0828 in the same study. Such highly detailed atomic-level structure-activity relationship provides an unparalleled understanding of the complex dynamics involved in protein-ligand interactions in Mac1. These dynamic interactions present valuable prospects for the development of structure-guided design strategies modulating the phosphate-binding subsite of Mac1.

Empirical studies have established that the backbone atoms of Asp157 constitutes the oxyanion site of the viral Mac1²¹. The crystal structure of Mac1 bound to substrate ADP-ribose revealed a water mediated contact with the residue Asp157⁶. Therefore, targeting such an interaction offers a good therapeutic window for optimizing new compounds targeting viral Mac1. Experimental compounds like IAL-MD0131 are proposed targeting this structural feature⁶. Crystallographic studies conducted on compound ZINC000263392672 is found to be stabilizing the active site of viral Mac1 by contributing hydrogen bonding interaction via the pyrrolo pyrimidine fragment²¹. Crystal structure of Mac1 in complex with pyrrolo-pyrimidine analog demonstrated polar interaction with residue Asp157⁹⁷. Another experimental analysis on compound LRH-0003 co-crystallized with Mac1 demonstrated that the hydrazide carbonyl functional group of the compound forms an effective hydrogen bond with the main chain atoms of Asp157⁶. Interestingly, 8 compounds out of 12 from the current series shows interaction with Asp157. Therefore, improving the functional groups from the current series that interact with Asp157 can be a good starting point in optimizing the inhibitor potency.

The main chain atoms from Gly130 are experimentally validated to play a key role in the viral Mac1 inhibition. For instance, in case of compounds like IAL-MD0131 and aztreonam, the beta-lactam and sulfonic acid moieties are stabilized via water assisted contact with Gly130⁶. Another crystallographic study observed that the hydroxyl group of high activity compound Z8601 interacts with main chain nitrogen atoms of Gly130 via polar interaction in the form of a hydrogen bond¹⁰¹. Therefore, synthesis of molecules that focus on interacting with the backbone atoms of Gly130 can serve as a promising initial approach for achieving the highest level of inhibitory potency.

Val-49 is spatially located near the phosphate binding loop in Mac1. A crystallographic study targeted interaction with this residue¹⁰¹. As per the report, compound Z5331 was designed to interact with the backbone atom of Val49 via its methyloxadiazole functional group rather than the amino acid residues in the phosphate binding loop¹⁰¹. Such an approach can also be used as an alternative strategy for targeting viral Mac1 protein. Pro125 occupies a central position in the substrate binding pocket of the viral Mac1⁹⁷. Considering the strategic location of this residue, various inhibitors are designed targeting the interaction with Pro125. For example, aztreonam is repurposed to interact with the backbone atoms of Pro125 from oxyanion site via its carboxylic acid group⁶. Therefore, modifications in the functional group interacting with Val49 and Pro125 from the current series may offer a good strategy for compound activity optimization.

Cluster analysis results of compounds 7a and 7k reveals active interaction with Ala154 (see supplementary data). Ala154 also holds a strategic position in the Mac1's oxyanion region. Repurposed drug aztreonam is known to be stabilized by a hydrogen bond provided by the backbone atoms of Ala154⁶. Moreover, crystallographic data from Gahbauer et al., in their high resolution structure of Mac1 showcased the active involvement of water-mediated hydrogen bonds in stabilizing compound Z8539 through its amide functional group's interaction with Ala154¹⁰². Following this structural lead, the synthesis of compounds that specifically target interactions with the backbone atoms of Ala154 can be considered a promising initial strategy for achieving the highest possible level of inhibitory potency.

Compound 7d is one of the best compounds that was observed promising free energy towards Mac1. Cluster analysis of trajectory of this compound revealed a unique interaction with Leu127. This residue play a critical role in stabilization of the everted loop in maintaining the open state of the phosphate binding loop. In account of this critical function, numerous compounds like Z4305, F4769, and Z5531 are optimized targeting its interaction with the main chain atoms of Leu127. Interestingly the potency of these compounds was found to dramatically improve¹⁰¹. Such critical SAR data, thus opens a new therapeutic opportunity in activity optimization.

In short, the structural data presented in this report explores the functional dynamics and mechanistic rearrangements in the viral Mac1 and hence may help in drug development and therapeutic strategies that specifically

Molecule	7a	7i	7k	7 L	Standard
MW	298.38	367.27	330.4	360.88	174.2
GI absorption	High	High	High	High	High
Pgp substrate	No	No	No	Yes	No
CYP1A2 inhibitor	Yes	Yes	Yes	Yes	Yes
CYP2C19 inhibitor	Yes	Yes	Yes	Yes	No
CYP2C9 inhibitor	Yes	Yes	Yes	Yes	No
CYP2D6 inhibitor	Yes	No	No	No	No
CYP3A4 inhibitor	No	No	No	No	No
log K _p (cm/s)	-4.56	-4.08	-4.42	-3.97	-6.46
Lipinski rule violations	1	1	1	1	0
Ghose Rule violations	0	0	0	0	0
Veber rule violations	0	0	0	0	0
Egan Rule violations	0	0	0	0	0
Muegge rule violations	1	1	1	1	1
Bioavailability Score	0.55	0.55	0.55	0.55	0.55
PAINS alerts	0	0	0	0	0
Brenk alerts	0	0	0	0	0

Table 9. Summary of the ADMET analysis results.

target the Mac1 domain. By examining the potential inhibitors and their mechanisms of action, we aim to shed light on the feasibility of developing novel antiviral drugs that can specifically modulate the activity of this critical viral protein. As we discuss the intricate Mac1's structural dynamics, we hope to pave the way for innovative approaches in the management of the SARS-CoV-2 infections, offering new avenues for therapeutic intervention against COVID-19 and upcoming new variants. In this research paper, we offer the structural details of Mac1 that can act as a spring-board to initiate studies for exploring the structural and functional properties of Mac1. We thus highlight the potential it holds as a druggable target for the development of innovative antiviral therapies.

ADMET study

The results obtained from the ADMET analysis are summarized in Table 9.

Overall, all the ADMET profiles of compounds 7a, 7i, 7k, and 7 L exhibit favorable ADMET properties as compared to the standard crystallographic compound as a reference, suggesting their potential suitability for drug development. They show high gastrointestinal absorption, and interactions with key enzymes. It's important to note the absence of Ghose, Veber, Egan, or Muegge rule violations, further supporting their potential as drug candidates. It is to be noted that, none of the compounds flags PAINS and Brenk alerts. PAINS alerts are associated with substructures that have been identified as common in compounds that often show false-positive results in high-throughput screens¹⁰². A lack of PAINS alerts suggests that the compounds do not contain structural motifs known to interfere with assay readouts. This is advantageous as it reduces the likelihood of misleading or inaccurate results in experimental assays. Similarly, Brenk alerts are related to undesirable chemical features that may impact the biological activity or behavior of a compound¹⁰³. The absence of Brenk alerts is considered favorable, indicating that the compounds do not possess problematic structural characteristics that could hinder their development¹⁰⁴. To sum up, zero PAINS and Brenk alerts suggest that the compounds have a lower likelihood of causing interference or exhibiting problematic behavior in biological assays. This is a positive indication for the potential reliability and suitability of the compounds for further drug development studies.

Toxicity study

The toxicity prediction analysis conducted for promising compounds 7a, 7i, 7k, and 7 L revealed varied outcomes across different endpoints. The toxicity radar charts of the compounds are summarized in the supplementary material. Notably, Compound 7a, 7i, 7k, and 7 L exhibited activity in neurotoxicity, respiratory toxicity, BBB-barrier permeability, and ecotoxicity, suggesting potential adverse effects on the nervous system, respiratory system, blood-brain barrier integrity, and environmental health. Conversely, the compound showed inactivity in hepatotoxicity, nephrotoxicity, cardiotoxicity, carcinogenicity, immunotoxicity, mutagenicity, and several molecular initiating events, implying a lower risk of adverse effects in these domains. Metabolically, compound 7a, 7i, 7k, and 7 L demonstrated mixed activity across cytochrome P450 enzymes, indicating potential interactions with drug metabolism pathways. The toxicity prediction provided here underscore the importance of predictive toxicology in early-stage compound evaluation, facilitating informed decision-making and risk mitigation strategies in the further activity optimization and lead development processes.

Conclusion

We have reported an efficient and convenient procedure for the regioselective synthesis of pyrazoline derivatives. This method is very simple where regioisomer separation is not necessary. The starting material required for the preparation of β -amino ketones can be made available in any organic laboratory and its purification does not

require any column separation. The protocol presented in the current paper for the preparation of pyrazoline is applicable to a wide range of substrates and demonstrated tolerance to a variety of functional groups. Pyrazolines can be conveniently dehydrogenated using the methodology adopted in this report. Here we addressed the issue of selective conversion of double bond-protected chalcones into pyrazoline compounds through a reaction involving β -amino ketone and phenyl hydrazine hydrochloride that is scarcely reported in the recent literature. Based on endpoint methods of free energy estimation, it appears the compounds 7a, 7d, 7 g, 7i, 7k, and 7 L have enormous potential to be experimentally tested and further modified for activity optimization. Here we speculated the possible interactions that pyrazoline derivatives may form with the Mac1 from SARS-CoV-2. Results from various analyses, such as RMSD, RMSF, RG, and SASA, conducted in this study, support the idea that the synthesized compounds may form a conformationally stable complex with the viral Mac1. The ADMET analysis conducted in this study detected favorable odds for further optimization of this series of compounds. The comprehensive in silico toxicity assessment provides valuable insights into the safety profile of compound 7a, 7i, 7k, and 7 L. While it exhibits concerning activity in certain endpoints like neurotoxicity and respiratory toxicity, its inactivity in crucial areas such as hepatotoxicity and carcinogenicity suggests potential suitability for further development pending additional studies. We implemented various forms of interaction analysis techniques like analysis of docking poses, cluster analysis of MD simulation, hydrogen bonding analysis and manual distance-based analysis in this study. The main objective was to explore the maximum possible interaction space these newly synthesized chemical compounds can experience in the viral Mac1 protein. At this end, we can conclude that using multiple techniques appears to be advantageous in the identification of various interactions that can be easily missed if relied on a single interaction analysis method. Although these compounds can be potentially used for controlling the replication of SARS-CoV-2 by inhibiting the macrodomain, the results presented here are still speculations and are further needed to be experimentally verified. At the same time, we provide rich interaction details along with its structural and functional significance that in itself offers merit for further exploration of this chemical scaffold in SARS-CoV-2 therapeutics.

Data availability

The data generated and analyzed during the current study are available from the corresponding author on reasonable request.

Received: 8 January 2024; Accepted: 28 November 2024

Published online: 04 January 2025

References

- Dhamo, K. et al. Global emerging omicron variant of SARS-CoV-2: impacts, challenges and strategies. *J. Infect. Public. Health* **16** (1), 4–14 (2023).
- Cheia, C. et al. Macrodomain Mac1 of SARS-CoV-2 nonstructural protein 3 hydrolyzes diverse ADP-ribosylated substrates. *bioRxiv* (2023).
- Ayipo, Y. O. et al. Molecular modelling and structure-activity relationship of a natural derivative of o-hydroxybenzoate as a potent inhibitor of dual NSP3 and NSP12 of SARS-CoV-2: in silico study. *J. Biomol. Struct. Dyn.* **41** (5), 1959–1977 (2023).
- Khodavardipour, A. et al. Concise update on genomics of COVID-19: Approach to its latest mutations, escalated contagiousness, and vaccine resistance. *Glob. Med. Genet.* **8** (3), 85–89 (2021).
- Qin, B. et al. Identification of the SARS-unique domain of SARS-CoV-2 as an antiviral target. *Nat. Commun.*, **14** (2023).
- Schuller, M. et al. Discovery and Development Strategies for SARS-CoV-2 NSP3 macrodomain inhibitors. *Pathogens* **12** (2), 324 (2023).
- Correy, G. J. et al. The mechanisms of catalysis and ligand binding for the SARS-CoV-2 NSP3 macrodomain from neutron and x-ray diffraction at room temperature. *Sci. Adv.* **8** (21) (2022).
- Lei, X. et al. Activation and evasion of type I interferon responses by SARS-CoV-2. *Nat. Commun.* **11** (1), 3810 (2020).
- Alhammad, Y. M. et al. SARS-CoV-2 Mac1 is required for IFN antagonism and efficient virus replication in cell culture and in mice. *Proc. Natl. Acad. Sci. U. S. A.* **120**(35) (2023).
- Kumar, R. et al. Synthetic approaches, Biological activities, and structure-activity relationship of pyrazolines and related derivatives. *Top. Curr. Chem. (Cham.)* **381** (3), 12 (2023).
- Varghese, B. et al. Unveiling a versatile heterocycle: pyrazoline - a review. *RSC Adv.* **7**, 46999–47016 (2017).
- Chandra, T. Synthesis of substituted acridinyl pyrazoline derivatives and their evaluation for anti-inflammatory activity. *Eur. J. Med. Chem.* **45**, 1772–1776 (2010).
- Karabacak, M. et al. Synthesis and evaluation of new pyrazoline derivatives as potential anticancer agents. *Molecules* **20** (10), 19066–19084 (2015).
- Ardiansah, B. Pharmaceutical importance of pyrazoline derivatives: a mini review. *J. Pharm. Sci. Res.* **9**, 1958–1960 (2017).
- Nehra, B. et al. Recent advancements in the development of bioactive pyrazoline derivatives. *Eur. J. Med. Chem.* **205**, 112666 (2020).
- Matiadis, D. & Sagnou, M. Pyrazoline hybrids as promising anticancer agents: an up-to-date overview. *Int. J. Mol. Sci.* **21** (15), 5507 (2020).
- Mehmood, R. et al. Synthesis and evaluation of 1,3,5-Triaryl-2-pyrazoline derivatives as potent dual inhibitors of urease and α -glucosidase together with their cytotoxic, molecular modeling and drug-likeness studies. *ACS Omega* **7** (4), 3775–3795 (2022).
- Moon, P. et al. Discovery of potent pyrazoline-based covalent SARS-CoV-2 main protease inhibitors. *Chembiochem* **24**(11), e202300116 (2023).
- Akman, S. et al. Density functional modeling, and molecular docking with SARS-CoV-2 spike protein (Wuhan) and omicron S protein (variant) studies of new heterocyclic compounds including a pyrazoline nucleus. *J. Biomol. Struct. Dyn.* **41** (22), 12951–12965 (2023).
- Shahabuddin et al. Reaction of 7 α -bromo-6-nitrocholest-5-enes with hydrazine: formation of steroid pyrazolines and molecular docking against SARS-CoV-2 omicron protease. *Steroids* **188**, 109120 (2022).
- Schuller, M. et al. Fragment binding to the Nsp3 macrodomain of SARS-CoV-2 identified through crystallographic screening and computational docking. *Sci. Adv.* **7** (16), eabf8711 (2021).
- Li, J. T., Zhang, X. H. & Lin, Z. P. An improved synthesis of 1,3,5-triaryl-2-pyrazolines in acetic acid aqueous solution under ultrasound irradiation. *Beilstein J. Org. Chem.* **3**, 13 (2007).
- Karrouchi, K. et al. Synthesis and pharmacological activities of pyrazole derivatives: a review. *Molecules* **23** (1), 134 (2018).

24. Nigst, T. A., Antipova, A. & Mayr, H. Nucleophilic reactivities of hydrazines and amines: the futile search for the α -effect in hydrazine reactivities. *J. Org. Chem.* **77** (18), 8142–8155 (2012).
25. Gupta, R., Gupta, N. & Jain, A. Improved synthesis of chalcones and pyrazolines under ultrasonic irradiation. *Indian J. Chem.* **49B**, 351 (2010).
26. Kidwai, M., Kukreja, S. & Thakur, R. K2CO3-Mediated regioselective synthesis of isoxazoles and pyrazolines Lett. *Org. Chem.* **3**, 135 (2006).
27. Zahran, M. A. H. et al. Efficient microwave irradiation enhanced stereoselective synthesis and antitumor activity of indolylchalcones and their pyrazoline analogs. *J. Chem. Sci.* **122**, 587–595 (2010).
28. Goyal, A., Sharma, S. & Gaba, J. Microwave assisted synthesis of some novel pyrazoline derivatives as potential antifungal agents. *Indian J. Chem.* **56B**, 334 (2017).
29. Malhotra, V. et al. Substituted imidazole derivatives as novel cardiovascular agents. *Indian J. Chem.* **41B**, 1310 (2002).
30. Tiwari, A. K. et al. Synthesis, characterization and in vitro antimicrobial activity of some novel 4, 5-dihydro-1H-pyrazoline derivatives. *Indian J. Chem.* **56B**, 317 (2017).
31. Fazaeli, R. H. Highly efficient catalysts for the synthesis of Novel 1,3,5- triaryl-2-Pyrazoline derivatives. *Open Catal. J.* **3**, 79 (2010).
32. Paul, S., Pradhan, K. & Das, A. R. Ethyl lactate as a green solvent: a promising bio-compatible media for organic synthesis. *Green. Chem.* **3**, 111 (2016).
33. Holla, B. & Mahalinga, M. Synthesis of pyrazolines promoted by amberlyst-15 catalyst. *Indian J. Chem.* **45B**, 568 (2002).
34. Sridhar, S. & Rajendraprasad, Y. Synthesis and analgesic studies of some New 2 pyrazolines. *E J. Chem.* **9**, 1810 (2012).
35. Bhat, P., Shridhar, G., Ladage, S. & Ravishankar, L. An eco-friendly synthesis of 2-pyrazoline derivatives catalysed by CeCl₃·7H₂O. *J. Chem. Sci.* **129**, 1441 (2017).
36. Uzma, N. et al. Impact of Organic solvents and Environmental pollutants on the Physiological Function in petrol filling workers. *Int. J. Environ. Res. Public. Health* **5**, 139 (2008).
37. Lokhande, P. D., Waghmare, B. Y. & Sakate, S. S. Regioselective one-pot synthesis of 3,5-diarylpypyrazoles. *Indian J. Chem.* **44B**, 2338–2342 (2005).
38. Meshram, R. J. et al. Known compounds and new lessons: structural and electronic basis of flavonoid-based bioactivities. *J. Biomol. Struct. Dyn.* **38** (4), 1168–1184 (2020).
39. Meshram, R. J. et al. Pharmacophore mapping approach for drug target identification: a chemical synthesis and in silico study on novel thiadiazole compounds. *J. Clin. Diagn. Res.* **11** (5), KF01–KF08 (2017).
40. Meshram, R. J. et al. Sequence analysis and homology modeling of laccase from pycnoporus cinnabarinus. *Bioinformation* **5** (4), 150–154 (2010).
41. Patil, K. K. et al. Dietary flavonoids inhibit the glycation of lens proteins: implications in the management of diabetic cataract. *3 Biotech.* **9** (2), 47 (2019).
42. Cousins, K. R. Computer review of ChemDraw Ultra 12.0. *J. Am. Chem. Soc.* **133** (21), 8388 (2011).
43. O’Boyle, N. M. et al. Open babel: an open chemical toolbox. *J. Cheminform.* **3**, 33 (2011).
44. Rappe, A. K. et al. UFF, a full periodic table force field for molecular mechanics and molecular dynamics simulations. *J. Am. Chem. Soc.* **114**, 10024–10039 (1992).
45. Dallakyan, S. & Olson, A. J. Small-molecule library screening by docking with PyRx. *Methods Mol. Biol.* **1263**, 243–250 (2015).
46. Kaplan, W. & Littlejohn, T. G. Swiss-PDB viewer (deep view). *Brief. Bioinform.* **2** (2), 195–197 (2001).
47. Huey, R. et al. A semiempirical free energy force field with charge-based desolvation. *J. Comput. Chem.* **28** (6), 1145–1152 (2007).
48. Morris, G. M. et al. AutoDock4 and AutoDockTools4: automated docking with selective receptor flexibility. *J. Comput. Chem.* **30** (16), 2785–2791 (2009).
49. Meshram, R. J. et al. Modeling and simulation study to identify threonine synthase as possible drug target in leishmania major. *Mol. Divers.* **25** (3), 1679–1700 (2021).
50. Phillips, J. C. et al. Scalable molecular dynamics on CPU and GPU architectures with NAMD. *J. Chem. Phys.* **153** (4), 044130 (2020).
51. MacKerell, A. D. et al. All-atom empirical potential for molecular modeling and dynamics studies of proteins. *J. Phys. Chem. B* **102** (18), 3586–3616 (1998).
52. MacKerell, A. D., Jr, Feig, M. & Brooks, C. L. 3rd Extending the treatment of backbone energetics in protein force fields: limitations of gas-phase quantum mechanics in reproducing protein conformational distributions in molecular dynamics simulations. *J. Comput. Chem.* **25** (11), 1400–1415 (2004).
53. Zoete, V. et al. SwissParam: a fast force field generation tool for small organic molecules. *J. Comput. Chem.* **32** (11), 2359–2368 (2011).
54. Spivak, M. et al. VMD as a platform for interactive small molecule preparation and visualization in quantum and classical simulations. *J. Chem. Inf. Model.* **63** (15), 4664–4678 (2023).
55. Pronk, S. et al. GROMACS 4.5: a high-throughput and highly parallel open-source molecular simulation toolkit. *Bioinformatics* **29** (7), 845–854 (2013).
56. Pedretti, A. et al. The VEGA suite of programs: an versatile platform for cheminformatics and drug design projects. *Bioinformatics* **37** (8), 1174–1175 (2021).
57. Liu, H. & Hou, T. CaFE: a tool for binding affinity prediction using end-point free energy methods. *Bioinformatics* **32** (14), 2216–2218 (2016).
58. Friesner, R. A. et al. Extra precision glide: docking and scoring incorporating a model of hydrophobic enclosure for protein-ligand complexes. *J. Med. Chem.* **49**, 6177–6196 (2006).
59. Jurrus, E. et al. Improvements to the APBS biomolecular solvation software suite. *Protein Sci.* **27** (1), 112–128 (2018).
60. Wang, E. et al. End-point binding free energy calculation with MM/PBSA and MM/GBSA: strategies and applications in drug design. *Chem. Rev.* **119** (16), 9478–9508 (2019).
61. de Amorim, H. L., Caceres, R. A. & Netz, P. A. Linear interaction energy (LIE) method in lead discovery and optimization. *Curr. Drug Targets* **9** (12), 1100–1105 (2008).
62. Li, J. et al. The VSGB 2.0 model: a next generation energy model for high resolution protein structure modeling. *Proteins* **79**, 2794–2812 (2011).
63. Daina, A., Michelin, O. & Zoete, V. SwissADME: a free web tool to evaluate pharmacokinetics, drug-likeness and medicinal chemistry friendliness of small molecules. *Sci. Rep.* **3**, 742717 (2017).
64. Majrashi, T. A. et al. DFT and molecular simulation validation of the binding activity of PDE δ inhibitors for repression of oncogenic k-Ras. *PLoS ONE* **19** (3), e0300035 (2024).
65. Serag, M. I. et al. New oxadiazole and pyrazoline derivatives as anti-proliferative agents targeting EGFR-TK: design, synthesis, biological evaluation and molecular docking study. *Sci. Rep.* **14** (1), 5474 (2024).
66. Drwal, M. N. et al. ProTox: a web server for the in silico prediction of rodent oral toxicity. *Nucleic Acids Res.* **42** W53–58 (2014).
67. Roy, A. et al. Discovery of compounds that inhibit SARS-CoV-2 Mac1-ADP-ribose binding by high-throughput screening. *Antiviral Res.* **203**, 105344 (2022).
68. Fehr, A. R., Jankevicius, G., Ahel, I. & Perlman, S. Viral macrodomains: Unique mediators of viral replication and pathogenesis. *Trends Microbiol.* **26** (7), 598–610 (2018).

69. Michalska, K. et al. Crystal structures of SARS-CoV-2 ADP-ribose phosphatase: from the apo form to ligand complexes. *IUCrJ* **7**, 814–824 (2020).
70. Trott, O. & Olson, A. J. AutoDock vina: improving the speed and accuracy of docking with a new scoring function, efficient optimization, and multithreading. *J. Comput. Chem.* **31** (2), 455–461 (2010).
71. Du, X. Insights into protein-ligand interactions: mechanisms, models, and methods. *Int. J. Mol. Sci.* **17** (2), 144 (2016).
72. Blue, T. C. & Davis, K. M. Computational approaches: An underutilized tool in the quest to elucidate radical SAM dynamics. *Molecules* **26** (9), 2590 (2021).
73. Tiwari, N. P., Pandey, J. P. & Pandey, D. M. Protein-protein docking and molecular dynamics studies of sericin and cocoonase of silkworm: an insight for cocoon softening. *J. Biomol. Struct. Dyn.* **41** (4), 1193–1205 (2023).
74. Nouri Barkestani, M. et al. Optimization of IL-1RA structure to achieve a smaller protein with a higher affinity to its receptor. *Sci. Rep.* **12** (1), 7483 (2022).
75. Baba, R. A. et al. Quercetin suppresses ROS production and migration by specifically targeting Rac1 activation in gliomas. *Front. Pharmacol.* **15**, 1318797 (2024).
76. Alzain, A. A. et al. Integrating computational methods guided the discovery of phytochemicals as potential Pin1 inhibitors for cancer: pharmacophore modeling, molecular docking, MM-GBSA calculations and molecular dynamics studies. *Front. Chem.* **12**, 1339891 (2024).
77. Xie, D. et al. Design, synthesis, and inhibitory activity of hydroquinone ester derivatives against mushroom tyrosinase. *RSC Adv.* **14** (9), 6085–6095 (2024).
78. Aulifa, D. L. et al. Elucidation of molecular interactions between drug-polymer in amorphous solid dispersion by a computational approach using molecular dynamics simulations. *Adv. Appl. Bioinform. Chem.* **17**, 1–19 (2024).
79. Gackowski, M. et al. Novel thiourea and oxime ether isosteviol-based anticoagulants: MD simulation and ADMET prediction. *Pharmaceuticals (Basel)* **17** (2), 163 (2024).
80. Genheden, S. & Ryde, U. The MM/PBSA and MM/GBSA methods to estimate ligand-binding affinities. *Expert Opin. Drug Discov.* **10** (5), 449–461 (2015).
81. Hou, T. et al. Assessing the performance of the MM/PBSA and MM/GBSA methods. 1. The accuracy of binding free energy calculations based on molecular dynamics simulations. *J. Chem. Inf. Model.* **24** (1), 69–82 (2011).
82. Wang, J. & Hou, T. Develop and test a solvent accessible surface area-based model in conformational entropy calculations. *J. Chem. Inf. Model.* **25** (5), 1199–1212 (2012).
83. Sun, H. et al. Assessing the performance of MM/PBSA and MM/GBSA methods. 5. Improved docking performance using high solute dielectric constant MM/GBSA and MM/PBSA rescoring. *Phys. Chem. Chem. Phys. Oct.* **28** (40), 22035–22045 (2014).
84. Piovesan, D., Minervini, G. & Tosatto, S. C. The RING 2.0 web server for high quality residue interaction networks. *Nucleic Acids Res.* **44** (W1), W367–W374 (2016).
85. DeFrees, K. et al. An empirical study of amide-heteroarene p-stacking interactions using reversible inhibitors of a bacterial serine hydrolase. *Org. Chem. Front.* **6** (11), 1749–1756 (2019).
86. Salonen, L. M. et al. Cation-pi interactions at the active site of factor xa: dramatic enhancement upon stepwise N-alkylation of ammonium ions. *Angew. Chem. Int. Ed. Engl.* **48** (4), 811–814 (2009).
87. Salonen, L. M. et al. Molecular recognition at the active site of factor Xa: cation-p interactions, stacking on planar peptide surfaces, and replacement of structural water (2012).
88. Schottel, B. L., Chifotides, H. T. & Dunbar, K. R. Anion-p interactions. *Chem. Soc. Rev.* **37**, 68–83 (2008).
89. Gamez, P., Mooibroek, T. J., Teat, S. J. & Reedijk, J. Anion binding involving pi-acidic heteroaromatic rings. *Acc. Chem. Res.* **40** (6), 435–444 (2007).
90. Wang, D. X. & Wang, M. X. Anion-pi interactions: generality, binding strength, and structure. *J. Am. Chem. Soc.* **135** (2), 892–897 (2013).
91. Auffinger, P. et al. Halogen bonds in biological molecules. *Proc. Natl. Acad. Sci. U. S. A.* **101** (48), 16789–16794 (2004).
92. Cavallo, G. et al. The halogen bond. *Chem. Rev.* **116** (4), 2478–2601 (2016).
93. Howard, E. I. et al. Ultrahigh resolution drug design I: details of interactions in human aldose reductase-inhibitor complex at 0.66 Å. *Proteins* **55** (4), 792–804 (2004).
94. Muzet, N. et al. Electrostatic complementarity in an aldose reductase complex from ultra-high-resolution crystallography and first-principles calculations. *Proc. Natl. Acad. Sci. U. S. A.* **100** (15), 8742–8747 (2003).
95. El-Kabbani, O. et al. Structure of human aldose reductase holoenzyme in complex with statin: an approach to structure-based inhibitor design of the enzyme. *Proteins* **50** (2), 230–238 (2003).
96. Arthur, D. E. & Uzairu, A. Molecular docking studies on the interaction of NCI anticancer analogues with human phosphatidylinositol 4,5-bisphosphate 3-kinase catalytic subunit. *J. King Saud Univ. Sci.* **34** (4), 1151–1166 (2019).
97. Brosey, C. A. et al. Targeting SARS-CoV-2 Nsp3 macrodomain structure with insights from human poly(ADP-ribose) glycohydrolase (PARG) structures with inhibitors. *Prog. Biophys. Mol. Biol.* **163**, 171–186 (2021).
98. Alhammad, Y. M. O. & Fehr, A. R. The viral macrodomain counters host antiviral ADP-ribosylation. *Viruses* **12** (4), 384 (2020).
99. Frick, D. et al. Molecular basis for ADP-ribose binding to the Mac1 domain of SARS-CoV-2 nsp3. *Biochemistry* **59** (28), 2608–2615 (2020).
100. Yang, X. et al. Molecular basis for the MacroD1-mediated hydrolysis of ADP-ribosylation. *DNA Repair. (Amst.)* **94**, 102899 (2020).
101. Gahbauer, S. et al. Iterative computational design and crystallographic screening identifies potent inhibitors targeting the Nsp3 macrodomain of SARS-CoV-2. *Proc. Natl. Acad. Sci. U. S. A.* **120** (2) (2023).
102. Alshehri, O. M. et al. Investigation of anti-nociceptive, anti-inflammatory potential and ADMET studies of pure compounds isolated from Isodon rugosus wall. ex Benth. *Front. Pharmacol.* **15**, 1328128 (2024).
103. Fakhry, M. M. et al. New thiazolyl-pyrazoline derivatives as potential dual EGFR/HER2 inhibitors: design, synthesis, anticancer activity evaluation and in silico study. *Molecules* **28** (21), 7455 (2023).
104. Latosińska, M. & Latosińska, J. N. Favipiravir Analogues as inhibitors of SARS-CoV-2 RNA-dependent RNA polymerase, combined quantum chemical modeling, quantitative structure-property relationship, and molecular docking study. *Molecules* **29** (2), 441 (2024).

Acknowledgements

Authors are thankful to the Researchers Supporting Project number (RSP2025R491), King Saud University, Riyadh, Saudi Arabia.

Author contributions

RJM and PD conceived the project idea. RJ, PL and HG designed and conducted chemical synthesis and characterization. BS, RJM, AK, BK, UY designed, conducted in silico part. PD and RJM supervised the project. AK, AA and NAA acquired funding. AK, AA, BK, UY and NAA software support. All authors analysed the data and wrote the manuscript.

Declarations

Competing interests

The authors declare no competing interests.

Additional information

Supplementary Information The online version contains supplementary material available at <https://doi.org/10.1038/s41598-024-81711-5>.

Correspondence and requests for materials should be addressed to P.L. or R.J.M.

Reprints and permissions information is available at www.nature.com/reprints.

Publisher's note Springer Nature remains neutral with regard to jurisdictional claims in published maps and institutional affiliations.

Open Access This article is licensed under a Creative Commons Attribution-NonCommercial-NoDerivatives 4.0 International License, which permits any non-commercial use, sharing, distribution and reproduction in any medium or format, as long as you give appropriate credit to the original author(s) and the source, provide a link to the Creative Commons licence, and indicate if you modified the licensed material. You do not have permission under this licence to share adapted material derived from this article or parts of it. The images or other third party material in this article are included in the article's Creative Commons licence, unless indicated otherwise in a credit line to the material. If material is not included in the article's Creative Commons licence and your intended use is not permitted by statutory regulation or exceeds the permitted use, you will need to obtain permission directly from the copyright holder. To view a copy of this licence, visit <http://creativecommons.org/licenses/by-nc-nd/4.0/>.

© The Author(s) 2024